EUROPEAN ORGANIZATION FOR NUCLEAR RESEARCH

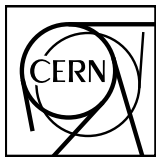

CERN-EP-2021-XXX
17 Nov 2021

Production of K^0_S, Λ ($\overline{\Lambda}$), $\Xi^{\pm}$ and $\Omega^{\pm}$ in jets and underlying events in pp and p–Pb collisions with ALICE

ALICE Collaboration*

Abstract

The production of strange hadrons (K^0_S, Λ, $\Xi^{\pm}$ and $\Omega^{\pm}$), baryon-to-meson ratios (Λ/K^0_S, Ξ/K^0_S and Ω/K^0_S) and baryon-to-baryon ratios (Ξ/Λ, Ω/Λ and Ω/Ξ) are measured ~~among inclusive, energetic jets and underlying events~~ inclusively, within energetic jets (JE), and within the so-called underlying event (UE) region in pp collisions at $\sqrt{s} = 13$ TeV and p–Pb collisions at $\sqrt{s_{\rm NN}} = 5.02$ TeV with the ALICE detector at the LHC. ~~For the first time, we present results on~~ The production of the multi-strange ~~particles ($\Xi^{\pm}$ and $\Omega^{\pm}$) and corresponding~~ particle and their ratios in jets and ~~underlying evens, providing an opportunity to test the strange particle production mechanism with a hard scattering. The~~ in the underlying event is measured for the first time. The transverse momentum ($p_{\rm T}$~~differential~~) distribution of hadrons ~~produced by jet is decrease slower than what is reported for inclusive one. The~~ associated with jets are significantly harder than that of the inclusive particle production. Concurrently, the baryon-to-meson and baryon-to-baryon ratios ~~in jets are clear different with the inclusive one in~~ measured in jets exhibit clear differences from values obtained from the inclusive spectra.This holds for both collision systems (pp and p–Pb) at the intermediate hadron $p_{\rm T}$~~range. On the contrary,~~ , while these ratios in ~~underlying events show the same behavior with the inclusive one. When comparing hadron spectra and ratios within different centrality bins, the jet one are found to independent on the centrality. The resultsof this paper provide significant~~ the UE region are similar to the inclusive ones. The event activity dependence is further investigated in different event classes classified with charged-particle multiplicity. No apparent event activity dependence is observed for particle production in jets in contrast to that in underlying events. These new results, compared to Monte Carlo event generators, provide strong evidence that the ~~jet fragmentation is not sufficient to describe~~ fragmentation of energetic jets alone is insufficient to describe the strange and multi-strange ~~particles~~ particle production in hadronic collisions at the LHC energies.

*See Appendix C for the list of collaboration members

1 Introduction

High-energy heavy-ion Production of identified hadrons via energetic hard parton fragmentations allows studying the interplay between hard partons and the soft-parton composited color-deconfined state of strongly-interacting matter, the quark-gluon plasma (A-A) collisions are expected to create a deconfined system with extreme temperature and density, the Quark-Gluon Plasma (QGP) [1–7], in which the degrees of freedom are partonic, rather than hadronic. The structure and dynamical behavior of the QGP arise at the microscopic level from the interactions between quarks and gluons described by Quantum Chromodynamics (QCD) [8–10]. The interpretation of the formed in (ultra-)relativistic high-energy heavy-ion results depends crucially on understanding results from small collisionssystems such as proton-proton() or proton-nucleus(p-A) . In collisions, there are not expected hot matter effects. So it is essential to investigate cold nuclear initial and final state effect to be used as the baseline for heavy-ion collisions [11, 12]. In (AA) collisions [13–17]. Species-dependent production of particles from the hard parton fragmentation is sensitive to hadronization processes in proton–proton (pp) collisions [18–21], and possibly influenced by cold-nuclear-matter (CNM) effects in proton–nucleus (pA) collisions, there are not any hot and cold nuclear initial- [22–24]. The common strategy to extract the information sensitive to the QGP medium is to compare the particle production in nucleus–nucleus collisions with that in pp and final-state effects. So it constitutes a baseline for the nuclear effects in both A-A and p-A collisions . proton–nucleus collisions. Therefore, for a long time, ppand proton–nucleus collisions are usually investigated as a reference for nucleus-nucleus collisions in the process of searching for the QGP and studying its properties.

Several collective phenomena In recent years, it becomes particularly imperative to study and understand the particle production mechanism in ppand pA collisions since several new features have been observed in high-multiplicity pp and p–Pb collisions that are reminiscent of the observation attributed to the creation of a medium in thermal and kinematic equilibrium in QGP in Pb–Pb collisions [25–31] [25–31]. These include the long-range angular correlations on the near and away side studiesof a trigger particle [26–28], non-vanishing v_2 coefficients 2nd order Fourier coefficients (v_2) in multi-particle cumulant studies, etc [25, 29]. In particular, in pp and p–Pb collisions, the baryon-to-meson ratios p/π and $\Lambda/\mathrm{K}^0_\mathrm{S}$ have manifest an enhancement at intermediate p_T (~ 3 GeV/c) [32–35] and the strange to non-strange hadron ratios have a significant enhancement with multiplicity [33, 35, 36], which is qualitatively similar to that observed in Pb–Pb collisions. The jet also constitute an important probe for the study of the QGP in heavy-ion collisions. On the contrarystrange to non-strange hadron ratio increases continuously as a function of charged-particle multiplicity density from low multiplicity ppto high multiplicity p–Pbcollisions and reaches the values observed in Pb–Pbcollisions [33, 35, 36]. It suggests the existence of a common underlying mechanism determining the chemical composition of particles produced in these three collision systems. On the other hand, several measurements show the absence of a robust nuclear effect on the jet production at mid-rapidity in small systems [37–44]. To better [37–45].

To understand particle production mechanisms in small collision systems, the charged-particle jets are used to probe particle generated by hard scattering and those of the separation of particle produced in hard processes (jet) from those of the underlying event is important. In a recent study, the ALICE Collaboration has studied baryon-to-meson ratios with a new method: by studying the ratios in two parts of the events separately – inside jets and in the event portion perpendicular to a jet cone in ppcollisions at $\sqrt{s} = 7$ TeVand p–Pbcollisions at $\sqrt{s_\mathrm{NN}} = 5.02$ TeV [46]. The results show that the $(\Lambda+\overline{\Lambda})/2\mathrm{K}^0_\mathrm{S}$ ratio enhancement at intermediate p_T observed previously in the inclusive particle measurements in Pb–Pbcollisions and in high multiplicity small system collisions is not caused by hard scatterings tagged by jets. In this contribution, the baryon-to-meson and multi-strange-to-strange particle ratios will be studied in charged-particle jets and in underlying events. It can help us to disentangle the will provide further insight into the contribution of soft and hard scattering contributions of processes to

the enhancement of the baryon-to-meson ~~or strange to non-strange enhancement~~ ratios enhancement at intermediate p_{T} and of the strange particle yields with multiplicity in small systems.

~~The baryon-to-meson ratios are sensitive to quark and gluon jet production in heavy-ion collisions.~~

In this paper, the production of $\mathrm{K}^0_{\mathrm{S}}$, Λ ($\overline{\Lambda}$), $\Xi^{\pm}$ and $\Omega^{\pm}$ in charged-particle jets and underlying events in ppcollisions at $\sqrt{s} = 13$ TeV and p–Pbcollisions at $\sqrt{s_{\mathrm{NN}}} = 5.02$ TeV is reported. ~~(Multi-)~~Strange particles are reconstructed in the pseudo-rapidity range $|\eta| < 0.75$. Jets ~~were~~ are reconstructed in the transverse momentum range $p_{\mathrm{T,jet}}^{\mathrm{ch}} > 10$ GeV/c and in the pseudo-rapidity range ~~$|\eta| < 0.75 - R$, where $R = 0.4$~~$|\eta| < 0.35$. The (multi-)strange particles associated with the jet are defined as a function of distance between particle ~~and jets~~ momentum and jet axis in $\eta - \varphi$ plane. The results presented in this paper significantly improve the precision ~~, also show the centrality classes dependent and extend to~~ of the p_{T}-differential measurements compared to ALICE previous one [46], including also the centrality dependence and extending to the multi-strange ~~particle sector , with respect to our previous measurements~~ sector in both pp (at different energy) and p–Pb collisions ~~[?]~~. The baryon-to-meson and baryon-to-baryon ratios in energetic jets are compared with the case of particles not associated with jets and ~~PYTHIA 8~~ PYTHIA 8 [47] simulation.

The paper is structured as follows. In Sec. 2, the ALICE apparatus and the data samples used for the analysis are presented. In Sec. 3, the ~~procedure adopted for charged~~ methods adopted for charged-particle jet reconstruction, (multi-)strange particle reconstruction, and particle-jet matching ~~strategy is~~ are described. The ~~systematic uncertainties associated with the measurement are also studied~~ estimation of the associated systematic uncertainties are reported in Sec. 3. The transverse momentum dependence of (multi-)strange hadron ~~with p_{T} differential distributions , particle ratioswith p_{T}~~ distributions and particle ratios, the model comparisons, and an interpretation of the results are presented and discussed in Sec. 4. ~~Finally, the paper is briefly summarised in Sec. 5~~.

2 ALICE ~~Detector~~ detector and data selection

A detailed description of the ALICE apparatus and its performance can be found in [48, 49]. This analysis ~~relied~~ relies on the central tracking ~~systems~~ system and the forward VZERO ~~system~~detector [50]. The ~~forward two~~ two forward scintillator arrays V0A (covering pseudo-rapidity range of $2.8 < \eta < 5.1$), and V0C ($-3.7 < \eta < -1.7$) were employed for both triggering ~~detectors and determining the~~ and event multiplicity class determination. The main central barrel detectors used for this analysis are the Inner Tracking System (ITS) [51], the Time Projection Chamber (TPC) [52] and the Time Of Flight detector (TOF) [53–56], which cover the pseudo-rapidity region $|\eta| < 0.9$ and ~~locate~~ are located inside a large solenoidal magnet providing a 0.5 T magnetic field.

The ITS, the innermost barrel detector~~is the ITS consisting~~ , consists of six cylindrical layers of ~~high-resolution silicon tracking detectors~~ high spatial resolution silicon detector using three different technologies. The two innermost layers~~are~~ (SPD) are based on silicon pixel technology ~~(SPD), covering~~ and cover $|\eta| < 2.0$ and $|\eta| < 1.4$, respectively. The SPD was used to reconstruct the collision's primary vertex and short track segments, which are called "tracklets". The four outer ~~layers are based on~~ ITS layers consist of silicon drift (SDD) and strip (SSD) detectors, with the outermost layer having a radius $r = 43$ cm. The SDD and SSD are able to measure the specific ionization energy loss ($\mathrm{d}E/\mathrm{d}x$) with a relative resolution around 10% in the low p_{T} region (up to ~ 1 GeV/c). The ITS is also used to reconstruct and identify low momentum particles down to 100 MeV/c that can not reach the TPC.

The TPC is a ~~sizeable~~ large cylindrical drift detector which is filled with a $\mathrm{Ne} - \mathrm{CO}_2$ gas mixture. The radius and the ~~longitude of TPC is~~ longitudinal dimensions of the TPC are about $85 < r < 250$ cm and $-250 < z < 250$ cm, respectively. As the main tracking device, the TPC provides full azimuthal acceptance for tracks in the pseudo-rapidity region $|\eta| < 0.9$. In addition, it provides charged-hadron

identification ~~information~~ via measurement of the specific ionization energy loss $\mathrm{d}E/\mathrm{d}x$. At low transverse momenta ($p_{\mathrm{T}} \lesssim 1.0$ GeV/c), the $\mathrm{d}E/\mathrm{d}x$ resolution of 5.2% for a minimum ionizing particle allows a track-by-track identification. ~~In contrast~~On the other hand, at high transverse momenta ($p_{\mathrm{T}} \gtrsim 2.0$ GeV/c), the overlapping energy loss ~~can still~~ has to be statistically distinguished ~~using~~ via a multi-Gaussian fit to the $\mathrm{d}E/\mathrm{d}x$ distributions.

~~Outside of the TPC and~~ The TOF, located at a radius of ~~approximately 4 m , the TOF~~ 3.7 m outside of the TPC, measures the particles' ~~time-of-flight~~time of flight. The TOF is a cylindrical array of multi-gap resistive plate chambers with an intrinsic time resolution of 50 ps. It covers the pseudo-rapidity range $|\eta| < 0.9$ with ~~(almost)~~ full azimuthal acceptance. It can provide particle identification over a broad range at intermediate transverse momenta ($0.5 \lesssim p_{\mathrm{T}} \lesssim 2.7$ GeV/c). The total time-of-flight resolution, including the collision time resolution, is about 90 ps in pp~~collisions and approximately? in~~ and p–Pb collisions~~()~~ [57, 58].

Data of pp collisions at $\sqrt{s} = 13$ TeV and of p–Pb collisions at $\sqrt{s_{\mathrm{NN}}} = 5.02$ TeV~~is~~ are used in this analysis. The pp~~samples were~~ data sample was recorded in 2016–2017~~with ALICE. The~~ , the p–Pb sample ~~is collected in 2016~~in 2016 with ALICE detector, respectively. The data were collected with a minimum bias (MB) trigger requiring ~~a~~ at least one hit in both V0 scintillators in coincidence with proton bunches' arrival from both directions. Interaction vertices are reconstructed by the extrapolation of ITS track segments towards the nominal interaction point. Pile-up events, due to multiple interactions in the triggered bunch crossing, are removed by exploiting the correlation between the number of pixel hits and the number of SPD tracklets. In addition, the coordinate of the primary vertex along the beam direction is required to be within ± 10 cm with respect to the ALICE nominal interaction point~~(center of the ALICE detector)~~. After event selection, the pp~~samples consist~~ sample consists of 1.5 billion events. The ~~interaction probability per single bunch crossing ranges between 2% and 14%. The~~ integrated luminosity of $\mathscr{L}_{\mathrm{int}} = 9.38 \pm 0.47$ nb^{-1} based on the visible cross section observed by the V0 trigger was extracted from a van der Meer scan [59]. About 500 million events ~~of~~ from the p–Pb samples ~~are~~ were selected, which correspond to an integrated luminosity of ~~$\mathscr{L}_{\mathrm{int}} = 287$~~ $\mathscr{L}_{\mathrm{int}} = 295 \pm 11$ μb^{-1}, ~~with a relative uncertainty of 3.7% [60]~~ [61]. The p–Pb events were divided into three multiplicity classes based on the total ~~charged~~ charge deposited in the V0A (the Pb-going direction). The multiplicity intervals and their corresponding mean charged-particle density ($\mathrm{d}N_{\mathrm{ch}}/\mathrm{d}\eta$) measured at ~~midrapidity~~ mid-rapidity ($|\eta| < 0.5$) are given in Ref. [62].

3 Analysis

3.1 ~~Charged~~ Charged-particle jet reconstruction

~~In this analysis, the~~ The FastJet package [63] is used to find ~~jets using charged particles with the so-called~~ the charged-particle jets with the anti-k_{T} algorithm~~. The algorithm is a commonly known jet finding algorithm that starts the clustering with the highest momentum particles, in contrast to the k_{T} algorithm, which does the opposite. The introduction of the algorithm can be found in~~ [64]. Charged particles, which are used as ~~the jet reconstructioninputs~~input for jet reconstruction, are reconstructed ~~using~~ by using the ITS and TPC information. The charged particle tracks are selected in $|\eta_{\mathrm{trk}}| < 0.9$ (TPC acceptance)~~and $p_{\mathrm{T}} > 0.15$~~. The transverse momentum (p_{T}) of tracks should be larger than 0.15 GeV/c. The jet resolution parameter is $R = 0.4$~~and the~~ . The reconstructed jet clusters are selected in $|\eta_{\mathrm{jet}}| < 0.35$. ~~A cut on~~ These conditions ensure that the jet cone is fully overlapping with the acceptances of both charged-particle tracks and the strange particles ($|\eta| < 0.75$). A transverse momentum cut on the charged-particle jet~~p_{T} ($p_{\mathrm{T,jet}}^{\mathrm{ch}}$) is applied as~~ , $p_{\mathrm{T,jet}}^{\mathrm{ch}} > 10$ GeV/c, is applied to tag the hard scattering processes [46].

Besides the hard parton-parton interactions in the collisions, there is ~~also the soft contribution summarizing everything that did not correlate~~ the soft contributions which are not correlated with the hard ~~collisions~~scattering. The background density (ρ_{bkg}) determined from the k_{T} algorithm [65, 66] in pp~~collisions~~ is around

1 GeV/c rad^{-1} ~~and is not subtracted on jet-by-jet basis in collisions~~, which is negligible and not subtracted. In p–Pb collisions, the underlying background is larger. The reconstructed jet is therefore further corrected for contributions ~~form~~ from the underlying event to the jet momentum as

$$p_{\mathrm{T,jet}} = p_{\mathrm{T,jet}}^{\mathrm{rec}} - \rho_{\mathrm{bkg}} \cdot A_{\mathrm{jet}}, \tag{1}$$

where the $p_{\mathrm{T,jet}}^{\mathrm{rec}}$ is the reconstructed jet p_{T}, A_{jet} is the jet area and ρ_{bkg} is the event-by-event background density [67]. The A_{jet} is calculated using the ~~Fastjet algorithm with the ghost area~~ FastJet algorithm with a ghost area of 0.005 [68]. A method that is suitable for ~~combinatory jet background density ()~~ the background density estimation for sparse systems ~~circumvents circumventing~~ to circumvent the problems arising from using the ghost jets is introduced in [69]. The basic idea is to neglect the ghosts and instead account for the empty areas by introducing a factor correcting the background density for it. It can be implemented by the following ~~approach~~ formula

$$\rho_{\mathrm{bkg}} = C \cdot \mathrm{median}\{\frac{p_{\mathrm{T,i}}}{A_i}\}, \text{ with } C = \frac{\sum_j A_j}{A_{\mathrm{acc}}} \frac{\sum_j A_j}{A_{\mathrm{acc}}}. \tag{2}$$

~~Technically, the occupancy correction factor C is calculated as the ratio of~~ Where A_j is the area of each k_{T} jet ~~clusters built by pure ghosts overall k_{T} jet clusters~~with at least one real track, i.e. excluding ghosts and A_{acc} is the area of the charged-particle acceptance, namely $(2 \times 0.9) \times 2\pi$. This method has the advantage that it uses the median and takes empty areas into account~~and that it does not have conceptual problems like other methods~~. This method ~~can be~~ is further refined for the specific ~~use~~ case of p–Pb collisions. It ~~can be~~ is shown that the exclusion of the ~~first~~ two k_{T} jets with highest p_{T} from Eq. (2) is enhancing the background quality [70, 71].

3.2 Strange particles reconstruction

The strange particles $\mathrm{K}^0_{\mathrm{S}}$, Λ, $\overline{\Lambda}$, $\Xi^{\pm}$ and $\Omega^{\pm}$ are reconstructed at mid-rapidity ($|\eta| < 0.75$) ~~with~~ via their specific weak decay topology. The following charged decay channels are ~~studied [72].~~ used [72]:

$$\begin{aligned}
\mathrm{K}^0_{\mathrm{S}} &\to \pi^+ + \pi^- & B.R. &= (69.20 \pm 0.05)\%, \\
\Lambda(\overline{\Lambda}) &\to \mathrm{p}(\overline{\mathrm{p}}) + \pi^-(\pi^+) & B.R. &= (63.9 \pm 0.5)\%, \\
\Xi^-(\overline{\Xi}^+) &\to \Lambda(\overline{\Lambda}) + \pi^-(\pi^+) & B.R. &= (99.887 \pm 0.035)\%, \\
\Omega^-(\overline{\Omega}^+) &\to \Lambda(\overline{\Lambda}) + \mathrm{K}^-(\mathrm{K}^+) & B.R. &= (67.8 \pm 0.7)\%.
\end{aligned}$$

The proton, pion, and ~~Kaon~~ kaon tracks (daughter tracks) are identified in the TPC via their measured energy deposition [49]. The identification ~~methods for~~ of the V^0 ($\mathrm{K}^0_{\mathrm{S}}$ and Λ ($\overline{\Lambda}$) which ~~decay~~ decays into two oppositely charged daughter particles) and cascade ($\Xi^{\pm}$ and $\Omega^{\pm}$ which ~~decay into a charged meson (bachelor)~~ decays into a bachelor charged meson plus a V^0 decaying particle, giving the ~~two-step process~~cascade decay topology) candidates follow those presented in earlier ALICE publications ~~[32, 36, 73? –75]~~[32, 36, 57, 73–75]. In addition, ~~to remove the contribution from~~ the contributions of pileup collisions outside the trigger proton bunch (“out-of-bunch pileup~~), it is requested~~ ”) should be removed. It is achieved by requiring that at least one of the ~~tracks from the decay products of the (multi-)strange hadron understudy is matched in~~ charged decay track matches a hit in a “fast” detector (either the ITS or ~~TOF detector~~the TOF detector). The selections used in this paper are summarized in Tab. A.1, A.2.

The signal extraction is performed as a function of p_{T}. In each p_{T} interval, an invariant mass histogram is ~~produced and~~ filled with the corresponding counts. Then a Gaussian function is used to fit the ~~peak~~signal, and a ~~liner~~ linear function is used to fit the ~~combinatory~~ combinatorial background. This allows for the extraction of the mean (μ) and width (σ) of the ~~peak~~signal. A “peak” region is defined within $\pm 6\sigma$

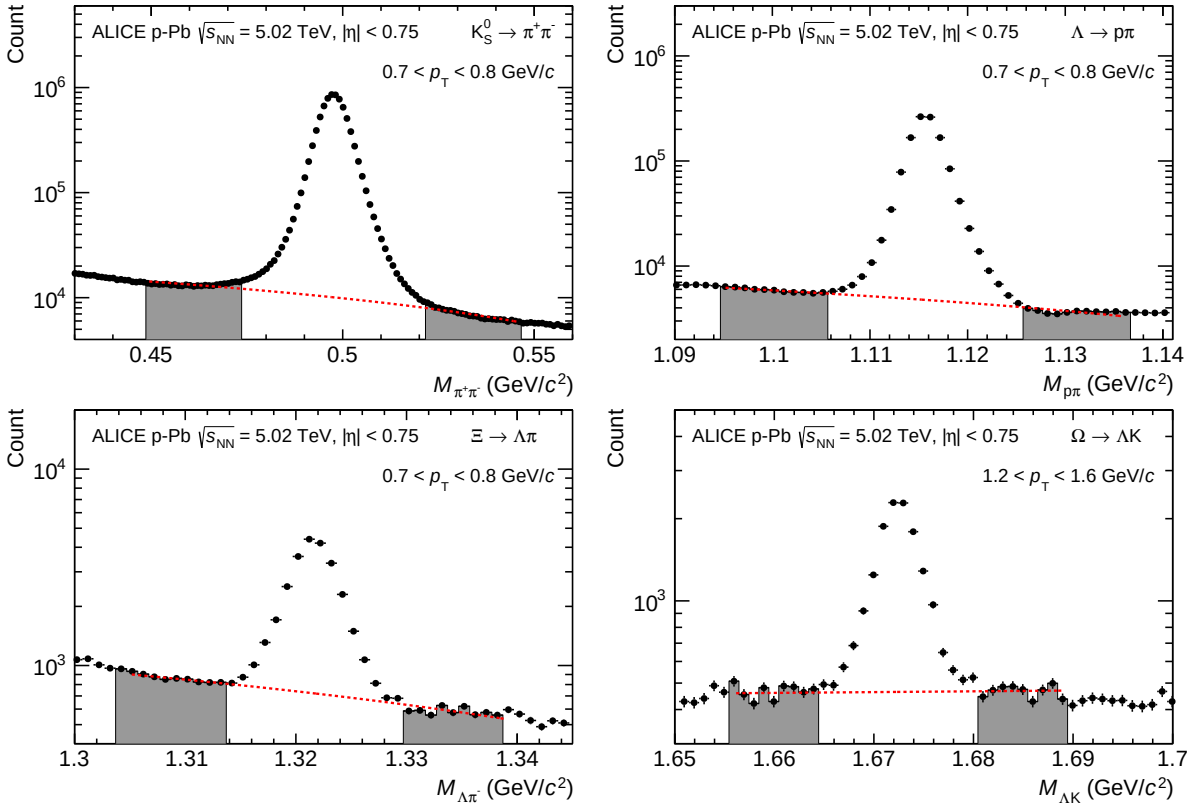

Figure 1: Invariant mass distribution for K^0_S, Λ, Ξ and Ω in different p_T intervals in MB p–Pbcollisions at $\sqrt{s_{NN}}$ = 5.02 TeV. The candidates are reconstructed in $|\eta| < 0.75$. The grey areas are used for background estimation applied in the signal extraction in the bin counting procedure.

for ~~V^0s~~ V^0s and $\pm 3\sigma$ ($\pm 4\sigma$) for cascades in pp (and p–Pb) with respect to μ for each p_T bin. The "background" regions are defined on both sides of ~~that central~~ the peak region. The p_T-differential yields of (multi-)strange particles are ~~extracted by fitting the background with a linear function extrapolated under the signal region~~ obtained by subtraction the integral of the background fit function in the peak region from the total bin counting in the same region. Examples of the invariant mass ~~peaks~~ signal for all particles are shown in ~~Fig.~~Figure 1. ~~Invariant Mass distribution for K^0_S, Λ, Ξ and Ω in different p_T intervals in MB system. The candidates are reconstructed in $|\eta| < 0.75$. The grey areas are used for signal extraction in the bin counting procedure. The red dashed lines represent the fit to the background distributions and the interpolate to the "peak" region.~~

3.3 Matching of strange particles to jets~~and underlying event~~

The strategy of ~~matching the~~ obtaining (multi-)strange ~~particles with jets follow those presented inearlier work [?]. The matching is done on a geometrical basis which presented in Eq. ??.~~

$$d(\text{particle},\text{jet}) = \sqrt{(\eta_{\text{particle}} - \eta_{\text{jet}})^2 + (\varphi_{\text{particle}} - \varphi_{\text{jet}})^2}$$

~~If the distance between the particle candidate and the jet (d) is smaller than the matching distance D (= 0.4), the candidate is considered to be inside the~~ hadrons associated to hard scatterings, tagged by charged-particle jets (JE particles), follows that presented in [46]. Particles are defined as located inside the jet ~~cone (JC). The raw yields in JC are not only composed of the hadron produced via jet fragmentation (write as JE), but also hadron from Underlying Event (UE)~~ cones (JC) if their distances to

the jet axis on the η–φ plane

$$R(\text{particle,jet}) = \sqrt{(\eta_{\text{particle}} - \eta_{\text{jet}})^2 + (\varphi_{\text{particle}} - \varphi_{\text{jet}})^2} \tag{3}$$

is less than a given value R_{max}, ~~which is defined as the sum of all particles which are not produced via hard parton fragmentation. The UE contribution is estimated by Perpendicular Cone~~

$$R(\text{particle,jet}) < R_{\text{max}}, \tag{4}$$

where $R_{\text{max}} = 0.4$ to be consistent with the value of the jet resolution parameter for jet reconstruction. The remaining contribution from the underlying event (UE) in the JC selection, which refers to particles not associated with jet fragmentation, is estimated in the perpendicular cone (PC) ~~yields. The PC indicates the cone, which is located in $\eta \times \varphi$ space in the perpendicular direction to the jet axis at the same~~ to the jet axis with radius $R = R_{\text{PC}}$. The values of $R_{\text{PC}} = 0.2$ and 0.6 are adopted to evaluate the UE estimation uncertainty.

Since the η~~. In addiction, the acceptance selections of inclusive (regardless of the association between particle and hard scattering), JC and UE (multi-)strange particles are different in the~~ –φ acceptances of the JC-selected particles differ from that for UE estimations, to subtract the UE component from the JC selection, a density distribution is defined

$$\frac{\mathrm{d}\rho}{\mathrm{d}p_{\text{T}}} = \frac{1}{N_{\text{ev}}} \times \frac{1}{A_{\text{acc}}} \times \frac{\mathrm{d}N}{\mathrm{d}p_{\text{T}}}, \tag{5}$$

where $\mathrm{d}N/\mathrm{d}p_{\text{T}}$ is the p_{T}-differential particle production yield, and N_{ev} and A_{acc} are the number of events and the area of the η–φ acceptance for a given selection. For JC and PC selections, N_{ev} corresponds to the number of events containing at least one jet with $p_{\text{T}} > 10$ GeV/c. The η–φ acceptance area, A_{acc}, is calculated via

$$A_{\text{acc}} = \alpha\pi R^2, \tag{6}$$

where R is the cone radius for the corresponding selection and α is a correction factor used to count the partial geometrical overlapping among jets on the η–φ plane. ~~To get the particle from JE the production yields are normalized to per-acceptance density (ρ).~~

$$\begin{aligned}
\text{Inclusive}: &\quad \frac{\mathrm{d}\rho}{\mathrm{d}p_{\text{T}}} = \frac{1}{N_{\text{ev}}} \times \frac{1}{\Delta\eta\Delta\varphi} \times \frac{\mathrm{d}N}{\mathrm{d}p_{\text{T}}} \\
\text{JC}: &\quad \frac{\mathrm{d}\rho}{\mathrm{d}p_{\text{T}}} = \frac{1}{N_{\text{ev}}^{\text{jet}}} \times \frac{1}{\mathscr{P}_{\text{JC}}\Delta\eta\Delta\varphi} \times \frac{\mathrm{d}N}{\mathrm{d}p_{\text{T}}} \\
\text{PC}: &\quad \frac{\mathrm{d}\rho}{\mathrm{d}p_{\text{T}}} = \frac{1}{N_{\text{ev}}^{\text{jet}}} \times \frac{1}{\mathscr{P}_{\text{PC}}\Delta\eta\Delta\varphi} \times \frac{\mathrm{d}N}{\mathrm{d}p_{\text{T}}}
\end{aligned}$$

The α factor is calculated via a Monte Carlo sampling approach using measured distributions of strange particles and jets as the inputs. The value is around 1.06 and insensitive to particle species and event multiplicities. It gives a minor correction on the particle density normalization since the production rate for jets in $p_{\text{T}} > 10$ GeV/$c$is rare even in high multiplicity p–Pbcollisions. With the normalization defined in Eq. (5), the p_{T}-differential production density distribution of JE particles is given by subtracting the density distribution of particles with the UE selection from that with the JC selection

$$\frac{\mathrm{d}\rho^{\text{JE}}}{\mathrm{d}p_{\text{T}}} = \frac{\mathrm{d}\rho^{\text{JC}}}{\mathrm{d}p_{\text{T}}} - \frac{\mathrm{d}\rho^{\text{UE}}}{\mathrm{d}p_{\text{T}}}. \tag{7}$$

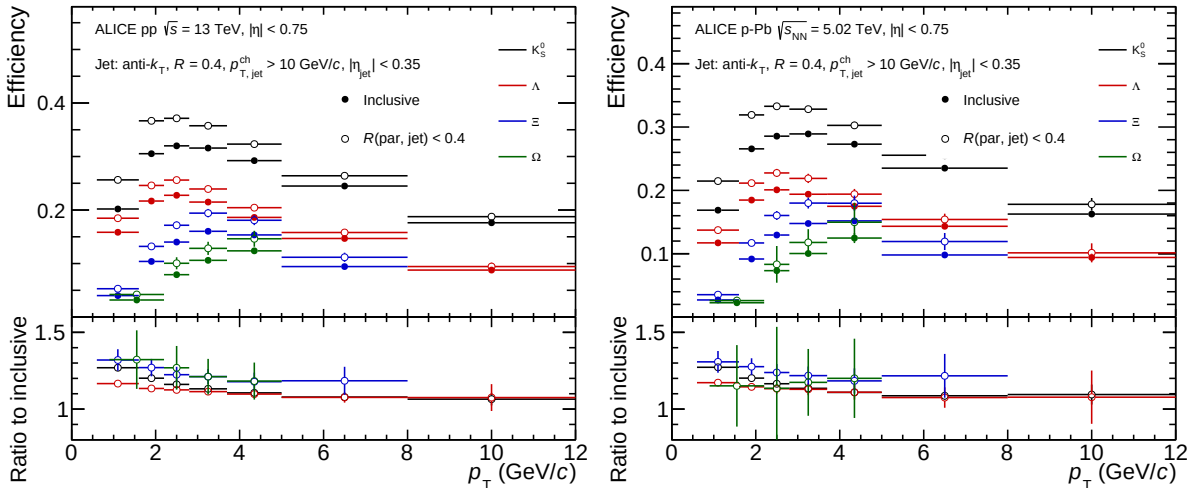

Figure 2: Strange particle reconstruction efficiency in ppcollisions at $\sqrt{s} = 13$ TeV(left) and in p–Pbcollisions at $\sqrt{s_{\rm NN}} = 5.02$ TeV(right) for two selections: inside jet cone, R(par, jet) < 0.4 and the inclusive one.

where the $\mathscr{P}$ denotes the probability of particles in a given selection found in the

In addition, to compare with the JE particles, the production yield of inclusive particles is also normalized according to Eq. (5). For the MB analysis, $N_{\rm ev}$ corresponds to the number of selected MB events. For the event activity-differential analysis in p–Pbcollisions, $N_{\rm ev}$ corresponds to the number of selected events in the corresponding event activity interval. The acceptance area, $A_{\rm acc}$, of inclusive particles is given by

$$A_{\rm acc} = \Delta\eta \times \Delta\varphi, \tag{8}$$

where $\Delta\eta = 2 \times 0.75$ and $\Delta\varphi = 2\pi$ rad, correspond to the η –and φ plane with respect to the inclusive oneacceptances of inclusive particles, respectively.

3.4 Corrections for strange particles reconstruction and feed-down

The reconstruction efficiency of particles are obtained in each particle is obtained from Monte Carlo simulated data. These are estimated using For this purpose PYTHIA 8.2 [47] and DPMJet [76] generators in pp and p–Pb, respectively, and tracsported through a GEANT 3 [77] collisions are used and the simulated data are propagated through the detector by GEANT3 [77] to simulate ALICE detector response. Due to different η-shape between particle in JC and the inclusive one, it is needed to take the η dependence of different particle distributions into account [**?**]. Fig.differences in the experimental acceptance for particles associated with jets and underlying events, the efficiencies of particles are estimated separately for each case [46]. Figure 2 shows the difference of reconstruction efficiency of JC particles selection particle and the inclusive one. The reconstruction efficiency for the particles in collisions at (left) and in collisions at (right) for two selections: inside jet cone, R(particle, jet) < 0.4 and the inclusive one.

Only the yields for Λ and $\overline{\Lambda}$ are significantly affected by secondary particles coming from the decays of charged and neutral Ξ baryons. The feed-down fraction is calculated with a data-driven approach [36]. The detailed of inclusive feed-down method has been introduced in previous ALICE analysis works [35, 75**?**]. In particular, the Λ and $\overline{\Lambda}$ in jet and UE feed-down component usually estimated by inclusive $\Xi^{\pm}$ spectra and PYTHIA simulations [**?**], due to lack of $\Xi^{\pm}$ in jet and UE results. In analyses [35, 57, 75]. In this work, the feed-down fraction in jets jet and UE is computed for each $p_{\rm T}$ bin by the measured spectra of $\Xi^{\pm}$ in jets and UEspectrajet and UE, thereby assuming that the production rates of charged and neutral Ξ are equal. Figure 3 shows the results of feed-down fraction in JC selection and the inclusive one.

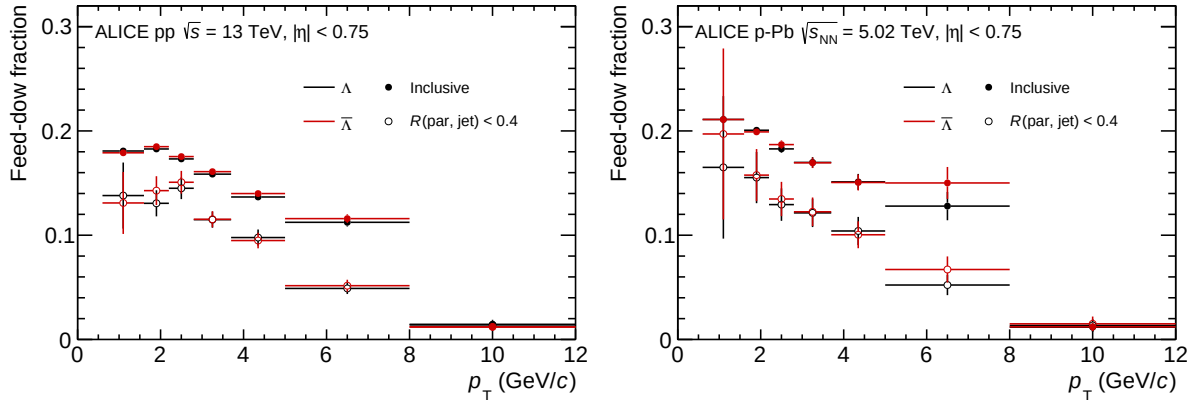

Figure 3: Fraction of Λ spectra removed due to feed-down subtraction of charged and neutral Ξ

Table 1: Main sources and values of the relative systematic uncertainties (%) of K^0_S, $\Lambda+\overline{\Lambda}$, $\Xi^-+\overline{\Xi}^+$ and $\Omega^-+\overline{\Omega}^+$ in pp collisions at $\sqrt{s}$ = 13 TeV. The values are reported for low, intermediate and high p_T.

Uncertainty source	K^0_S			$\Lambda+\overline{\Lambda}$			$\Xi^-+\overline{\Xi}^+$			$\Omega^-+\overline{\Omega}^+$		
p_T (GeV/c)	0.6	2	10	0.6	2	10	0.6	2	7	1	2	5
Detector material	4	4	4	4	4	4	4	4	4	4	4	4
Competing rejection	0.16	0.1	0.2	0	0.1	3.1	-	-	-	-	-	-
Track selection	1.5	1.2	0.4	0.6	1.4	1.3	2.8	0.1	0.	0.	1.5	0.2
Particle identification	0.1	0.1	0.1	0.3	0.2	1.1	1.9	1.7	2.4	3.9	8.7	6.
Proper lifetime	0	0.1	0	2.1	0.4	0	-	-	-	-	-	-
Topological	0.2	1.4	0	3.9	0.8	3.9	0.6	0.9	1.	2.8	5.4	2.4
Signal extraction	0.8	1.1	1.1	0.3	0.5	1.7	3.	1.	0.5	2.3	4.6	3
Total uncertainty	4.4	4.6	4.2	6.1	4.4	6.7	6.1	4.5	4.8	6.7	12.	8.2

3.5 Systematic uncertainties

~~The total~~ Total systematic uncertainty, for K^0_S, Λ, $\overline{\Lambda}$, $\Xi^\pm$ and $\Omega^\pm$ ~~reconstruction of each data point of the final results, due to the choice of selection criteria are~~ yields has been estimated separately in each p_T interval. Individual settings are loosened and tightened, in order to measure changes in the signal loss correction. The main sources of the systematic uncertainty in this measurements are related to the knowledge of detector materials, track selections, particle identification, proper lifetime, topological ~~selection~~ selections and signal extraction. All these individual error contributions, which are listed in ~~Tab.~~Table 1, 2 are added in quadrature.

Material budget. The effect of the incomplete knowledge of the detector's material budget is evaluated by comparing different Monte Carlo simulations in which the material budget was increased and decreased by 4.5%. This value corresponds to the uncertainty on the determination of the material budget by measuring photon conversions [49]. This particular systematic uncertainty is around ~~0.~~4%4% [57].

Competing rejection. The particle candidate should be rejected when the candidate mass can be calculated either under the K^0_Sor the Λ($\overline{\Lambda}$). To compute the uncertainty due to the competing selection, the analyis is redone with this rejection at 5 MeV/c^2 to 3 MeV/c^2 and 6 MeV/c^2 for the K^0_S. In the case of the Λor $\overline{\Lambda}$, the rejection can be removed entirely.

Track selection. To estimate the systematic uncertainty due to the track selection, the analysis has been

Table 2: Main sources and values of the relative systematic uncertainties (%) of K^0_S, $\Lambda+\overline{\Lambda}$, $\Xi^-+\overline{\Xi}^+$ and $\Omega^-+\overline{\Omega}^+$ in p–Pb collisions at $\sqrt{s_{NN}} = 5.02$ TeV. The values are reported for low, intermediate and high p_T values.

Uncertainty source	K^0_S			$\Lambda+\overline{\Lambda}$			$\Xi^-+\overline{\Xi}^+$			$\Omega^-+\overline{\Omega}^+$		
p_T (GeV/c)	0.6	2	10	0.6	2	10	0.6	2	7	1	2	5
Detector material	0.4	0.4	0.4	0.4	0.4	0.4	0.4	0.4	0.4	0.4	0.4	0.4
Competing rejection	0.16	0.3	0.5	0.1	0.	5.1	-	-	-	-	-	-
Track selection	1.4	1.7	1.8	0.2	1.3	1.4	0	0	0	1.3	2.5	0
Particle identification	0.1	0.2	0.2	0.3	0.2	1	3.1	1.2	0	8.1	13.7	5.9
Proper lifetime	0	0	0	1.6	0.3	0	0.6	0.4	0	0	3.3	0
Topological	4.4	0.6	1.9	3.9	0.9	2.7	1.3	0	2.6	1.2	4.8	3.7
Signal extraction	0.3	2.6	1.7	0.6	0.5	2.6	5.1	0.9	2.6	0	5.2	0
Total uncertainty	6.1	5.1	5.1	5.7	4.3	6.1	7.4	4.3	5.4	9.2	16.4	8

redone with ~~the~~ an increased number of required clusters in the TPC from default 70 points to 80 points.

Particle identification. The TPC dE/dx selection is used to reduce the combinatorial background in the (multi-)strange particle invariant mass distribution. The number of Gaussian σ in the identification of particles using the dE/dx ~~have been varied between~~ has been varied from 4σ to 6σ.

Proper ~~lifetime~~ decay length selection. The proper ~~lifetime defied~~ decay length is defined as mLc/p, ~~which~~ where m is the mass of the particles, L is the decay length, and p is the particle's momentum. The selection on the mLc/p is varied ~~from around~~ within 12 to 40 cm for K^0_S, 20 to 40 cm for Λ ($\overline{\Lambda}$)~~and $2c\tau$ to $6c\tau$~~, 10 to 30 cm for $\Xi^\pm$~~and~~, and 5 to 15 cm $\Omega^\pm$.

Topological selection. The values of the selection criteria ~~on~~ for the topological variables are varied within ranges leading to a maximum variation of $\pm$10% in the raw singal yied around their nominal values. The observed deviations for each component are summed in quadrature.

Signal extraction. In the same spirit, the signal extraction technique has been tested by varying the widths used to define the "signal" and "background" regions, expressed in terms of the number of σ as defined in Sec. 3.2. In particular the width of the peak region has been varied from the default value of 6σ to 7σ, 5σ and 4σ for V^0particles and 3σ to 4σ (3.5σ) and 2.5σ for $\Xi(\Omega)$.

The additional systematic uncertainty sources associated with particle yield in ~~jet are originated~~ the jet originate from the UE subtraction estimator and the jet p_T threshold. The systematic uncertainty due to the UE subtraction is estimated by varying the perpendicular cone radius from the chosen thresholds ~~from~~ of 0.4 (PC04) to 0.2 (PC02) and 0.6 (PC06). From the ~~deviation of~~ deviations obtained for different PC cone size, the relative systematic uncertainty of the UE subtraction is ~~obtained~~estimated. To estimate the effect of jet p_T ~~thresholds~~ threshold uncertainty, the analysis is repeated with the jet p_T cut 10 ± 1 GeV/c. The systematic ~~of the particle~~ uncertainties of particles in jets are added to the list of uncertainties in quadrature. The ~~value~~ values are shown in Table 3, 4.

The uncertainties of JE particle ratios (Λ/K^0_S, Ξ/K^0_S, Ω/K^0_S, Ξ/Λ, Ω/Λ and Ω/Ξ) also include three sources: the particle reconstruction, UE subtraction and the jet p_T threshold. The particle reconstruction uncertainty is propagated from the particle spectra. Uncertainties related to UE subtraction and jet p_T threshold are obtained by varying the same condition as particle spectra in both numerator and denominator of the corresponding ratios.

Table 3: Main sources and values of the relative systematic uncertainties (%) of particle p_{T}-differential density ($\mathrm{K}^0_{\mathrm{S}}$, $\Lambda+\overline{\Lambda}$, $\Xi^-+\overline{\Xi}^+$ and $\Omega^-+\overline{\Omega}^+$) and particle ratios ($\Lambda/\mathrm{K}^0_{\mathrm{S}}$, $\Xi/\mathrm{K}^0_{\mathrm{S}}$, $\Omega/\mathrm{K}^0_{\mathrm{S}}$, Ξ/Λ, Ω/Λ and Ω/Ξ) in JE in pp collisions at $\sqrt{s}$ = 13 TeV. The values are reported for low, intermediate and high p_{T}.

Uncertainty source	$\mathrm{K}^0_{\mathrm{S}}$			$\Lambda+\overline{\Lambda}$			$\Xi^-+\overline{\Xi}^+$			$\Omega^-+\overline{\Omega}^+$		
p_{T} (GeV/c)	0.6	2	10	0.6	2	10	0.6	2	7	1	2	5
Particle reconstruction	1.8	0.25	0.	5.5	0.6	0.	6.7	0.9	0.1	6	1.7	0.3
UE subtraction	0.1	0.1	0.1	0.1	0.2	0.1	1.5	0.2	0.3	3.6	1.8	0.5
Jet p_{T} threshold	0.6	3,1	10.9	0.6	1.1	9.9	3.5	2.4	5	0	0	0
Total uncertainty	1.8	3.1	10.9	5.6	1.2	9.9	7.7	2.6	5	7.1	2.5	0.6

Uncertainty source	$(\Lambda+\overline{\Lambda})/(2\mathrm{K}^0_{\mathrm{S}})$			$(\Xi^-+\overline{\Xi}^+)/(2\mathrm{K}^0_{\mathrm{S}})$			$(\Omega^-+\overline{\Omega}^+)/(2\mathrm{K}^0_{\mathrm{S}})$		
p_{T} (GeV/c)	0.6	2	10	0.6	2	7	1	2	5
Particle reconstruction	2.4	2.8	3.3	3.4	2.8	2.8	6.7	11.4	7.3
UE subtraction	0.8	0.2	0.4	3.5	0.2	0.1	10	4	2.2
Jet p_{T} threshold	0.4	2.3	1	1.7	1.6	3.6	1.	3.3	6.4
Total uncertainty	2.6	3.7	3.5	5.2	3.3	4.5	12.4	12.5	10

Uncertainty source	$(\Xi^-+\overline{\Xi}^+)/(\Lambda+\overline{\Lambda})$			$(\Omega^-+\overline{\Omega}^+)/(\Lambda+\overline{\Lambda})$			$(\Omega^-+\overline{\Omega}^+)/(\Xi^-+\overline{\Xi}^+)$		
p_{T} (GeV/c)	0.6	2	7	1	2	5	1	2	5
Particle reconstruction	3.4	3	3.2	6.7	11.5	7.5	6.8	11.5	7.4
UE subtraction	4.4	0.4	0.2	12.4	4.2	2.3	7.8	3.8	2.7
Jet p_{T} threshold	0.7	0.5	1.9	0.2	0.9	3.5	0.4	1.3	3
Total uncertainty	5.6	3	3.7	14.1	12.2	8.6	10.3	12.1	8.5

4 Results and discussion

4.1 Particle production and ratios in pp collisions at $\sqrt{s}$ = 13 TeV

For the strange hadrons discussed in this paper, the ratios of yields for particles and antiparticles are consistent with unity within uncertainties, as expected at the LHC energies in the midrapidity region. Therefore, all the spectra and the corresponding ratios shown in the following are reported after summing particles and antiparticles, when a distinct antiparticle state exists. The sums of particles and antiparticles, $\Lambda+\overline{\Lambda}$, $\Xi^-+\overline{\Xi}^+$ and $\Omega^-+\overline{\Omega}^+$ are also simply denoted as Λ, Ξ and Ω, unless explicitly written.

Figure 4 shows the fully corrected p_{T}-differential densities, $\mathrm{d}\rho/\mathrm{d}p_{\mathrm{T}}$ defined by eq. (5), of $\mathrm{K}^0_{\mathrm{S}}$, $\Lambda+\overline{\Lambda}$, Ξ and Ω obtained with various selections in pp collisions at $\sqrt{s}$ = 13 TeV. For particles matched to the jet cone, the JC-selected particles defined by eq. (4), the UE component estimated using the PC selection is mainly located at low-p_{T} in region of $p_{\mathrm{T}} < 1$–2 GeV/c. The UE fraction is higher for Λ, Ξ and Ω baryons than $\mathrm{K}^0_{\mathrm{S}}$ mesons. At the high-p_{T} ($>$ 2–4 GeV/c) region, the JC-selected particles are dominant by that within jets, the JE particles defined by eq. (7). The density distribution of UE particles rapid decreases with p_{T}, reaching values about an order of magnitude lower than that with the JC selection for particle p_{T} exceeding 4 GeV/c. This is consistent with the expectation that the high-p_{T} particles originate from jet fragmentation. The density distributions of the inclusive particles obtained in minimum-bias (MB) events are also compared with that of the JE and UE particles in figure 4. Due to the trigger of jets, the p_{T}-dependent density of JE particles is considerably less steep than inclusive particles. The density of UE particles is higher than that of inclusive particles since the former is obtained from events contain jets with $p^{\mathrm{ch}}_{\mathrm{T,jet}} > 10$ GeV/c. The p_{T} dependence of the density of inclusive particles is qualitatively similar to

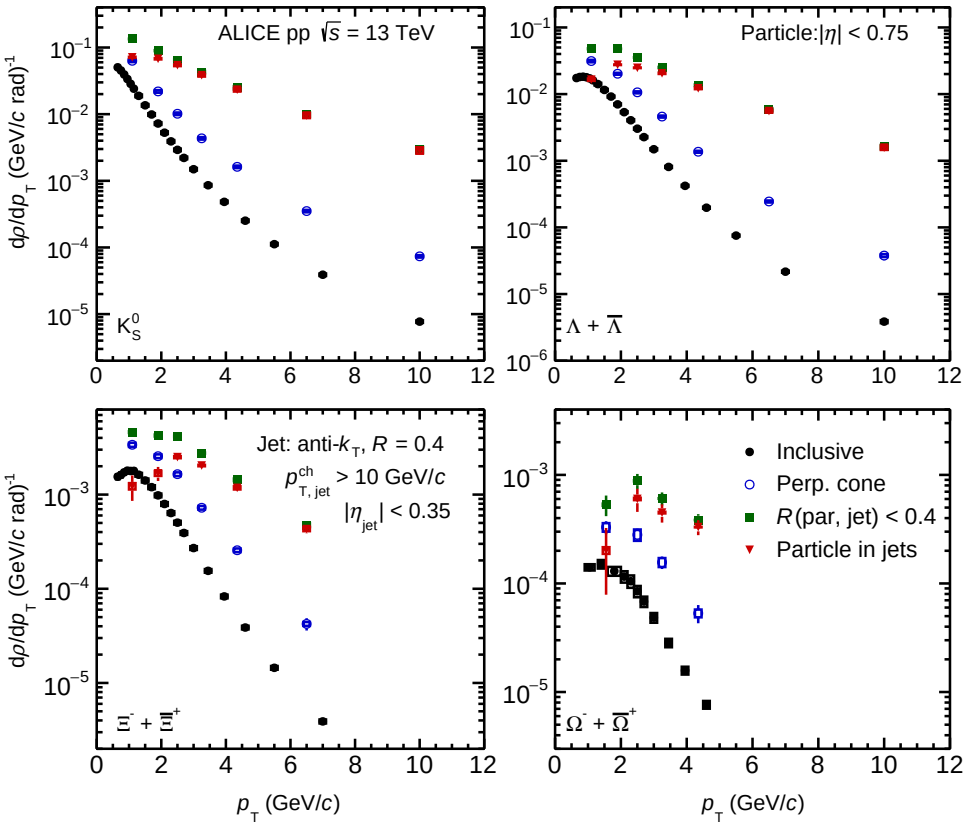

Figure 4: p_{T}-differential density, $\mathrm{d}\rho/\mathrm{d}p_{\mathrm{T}}$, of $\mathrm{K}^0_{\mathrm{S}}$ (top left panel), Λ (top right panel), Ξ (bottom left panel) and Ω (bottom right panel) in pp collisions at $\sqrt{s} = 13$ TeV. The spectra of JE particles (red inverted-triangle), associated with hard scatterings, are compared with that of JC (green squares) and UE (blue opened points) selections. The results from inclusive measurements (black closed points) are presented as well. The statistic uncertainties are represented by the vertical error bars, the systematic uncertainties are represented by the boxes.

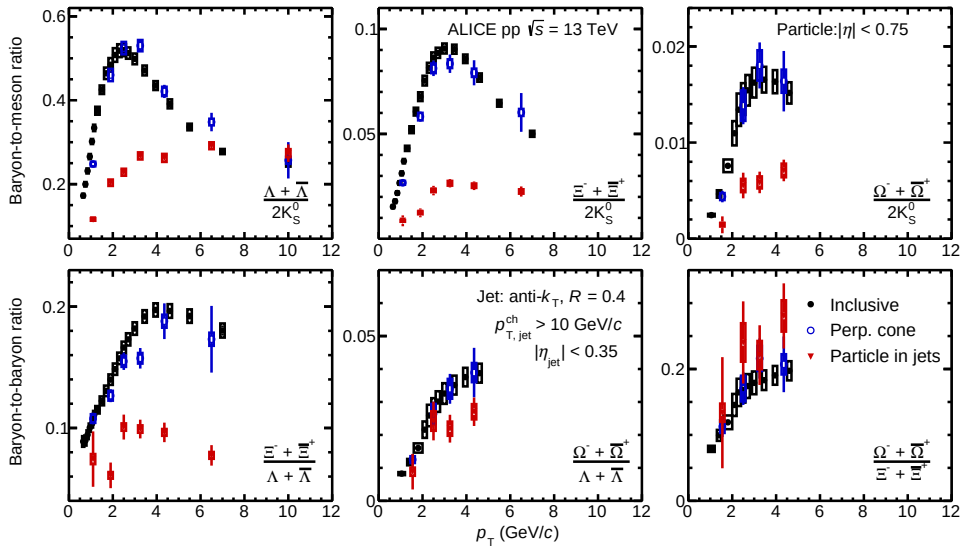

Figure 5: p_{T}-dependent strange baryon-to-meson (top) and baryon-to-baryon (bottom) ratios in pp collisions at $\sqrt{s} = 13$ TeV. For each case, the results of JE particles (red inverted-triangle) are compared with that of inclusive (black closed points) and UE (blue opened points) particles. See the text for details.

Table 4: Main sources and values of the relative systematic uncertainties (%) of particle p_{T}-differential density ($\mathrm{K}^0_{\mathrm{S}}$, $\Lambda+\overline{\Lambda}$, $\Xi^-+\overline{\Xi}^+$ and $\Omega^-+\overline{\Omega}^+$) and particle ratios ($\Lambda/\mathrm{K}^0_{\mathrm{S}}$, $\Xi/\mathrm{K}^0_{\mathrm{S}}$, $\Omega/\mathrm{K}^0_{\mathrm{S}}$, Ξ/Λ, Ω/Λ and Ω/Ξ) in JE in p–Pb collisions at $\sqrt{s_{\mathrm{NN}}} = 5.02$ TeV. The values are reported for low, intermediate and high p_{T}.

Uncertainty source	$\mathrm{K}^0_{\mathrm{S}}$			$\Lambda+\overline{\Lambda}$			$\Xi^-+\overline{\Xi}^+$			$\Omega^-+\overline{\Omega}^+$		
p_{T} (GeV/c)	0.6	2	10	0.6	2	10	0.6	2	7	1	2	5
Particle reconstruction	5	0.8	0	14.2	1.5	0	24.8	2.8	0.3	8.7	3.7	0.9
UE subtraction	0.3	0.1	0.1	0	0.1	11.2	14.1	0.8	0.7	0	0	1.2
Jet p_{T} threshold	0.3	3.5	11	3.2	1.8	0.1	24.9	3	4.1	3.1	10.7	7.6
Total uncertainty	5	3.6	11	14.6	2.3	11.2	37.9	4.2	4.1	9.3	11.3	7.7

Uncertainty source	$(\Lambda+\overline{\Lambda})/(2\mathrm{K}^0_{\mathrm{S}})$			$(\Xi^-+\overline{\Xi}^+)/(2\mathrm{K}^0_{\mathrm{S}})$			$(\Omega^-+\overline{\Omega}^+)/(2\mathrm{K}^0_{\mathrm{S}})$		
p_{T} (GeV/c)	0.6	2	10	0.6	2	7	1	2	5
Particle reconstruction	3.3	3.4	4.7	4.7	3.2	4	9.8	1.5	7.4
UE subtraction	0.8	0.1	0.1	9.1	1.8	1	4.1	0	0.3
Jet p_{T} threshold	1.4	2.6	0.1	8.6	2.4	6	0.5	1.5	0.3
Total uncertainty	3.7	4.3	4.7	13.4	4.4	7.2	10.6	15.1	7.4

Uncertainty source	$(\Xi^-+\overline{\Xi}^+)/(\Lambda+\overline{\Lambda})$			$(\Omega^-+\overline{\Omega}^+)/(\Lambda+\overline{\Lambda})$			$(\Omega^-+\overline{\Omega}^+)/(\Xi^-+\overline{\Xi}^+)$		
p_{T} (GeV/c)	0.6	2	10	0.6	2	7	1	2	5
Particle reconstruction	4.3	2.8	3.8	9.6	15	7.5	10	14.9	8.6
UE subtraction	9.9	1.9	0.8	3.6	0.1	0.3	11	1.8	0.1
Jet p_{T} threshold	2.7	0.6	2.6	0.4	5	3	0.4	3.8	1.7
Total uncertainty	11.1	3.4	4.7	10.3	15.8	8.1	14.9	15.5	8.7

the UE particles. Both of them show a strong, steeply falling with p_{T}.

The ratios of Λ, Ξ and Ω baryons to $\mathrm{K}^0_{\mathrm{S}}$ mesons are shown in the top three panels of figure 5, respectively, as a function of particle p_{T} in pp collisions $\sqrt{s} = 13$ TeV with different selection criteria. The ratios of UE particles giving by the PC selection are consistent with that of inclusive particles within uncertainties. They show an enhancement at p_{T} around 2–3 GeV/c with respective to the JE particles. The ratios of JE particles are approximately independent on p_{T} in the region beyond 2 GeV/c, in particular, they do not show a maximum at intermediate p_{T}. Clearly the enhancement of the ratio seen in the inclusive measurement is not present within jets. It is worth noting that the $\Lambda/\mathrm{K}^0_{\mathrm{S}}$ ratio of inclusive particles becomes consistent with that of JE particles within uncertainties in $p_{\mathrm{T}} > 6$ GeV/c as the high-p_{T} inclusive particles are composed of jet fragmentation. And the results of JE particles is consistent with that in [46] for pp collisions at $\sqrt{s} = 7$ TeV, showing collision energy independence. For the $\Xi/\mathrm{K}^0_{\mathrm{S}}$ and $\Omega/\mathrm{K}^0_{\mathrm{S}}$ ratios, even with limited p_{T} coverage due to lack of statistics, the trends imply that the results of inclusive measurements should be converged to that of JE particles at a higher p_{T}.

The strange baryon-to-baryon ratios, Ξ/Λ, Ω/Λ and Ω/Ξ, are presented in the bottom three panels of figure 5. For each case, the numerator always contains at least one more strange quark than the denominator, and the results obtained from different selection criteria are compared. Similar to the baryon-to-meson ratio shown in the upper three panels in this figure, the baryon-to-baryon ratios from the UE are consistent with that from the inclusive measurements within uncertainties. And in the measured p_{T} acceptance, they increase with p_{T} till 4 GeV/c. In $p_{\mathrm{T}} > 2$ GeV/c, the Ξ/Λ ratio of JE particles is almost independent on p_{T}, and shows a strong suppression by a factor of about 2 with respect to the inclusive measurements.

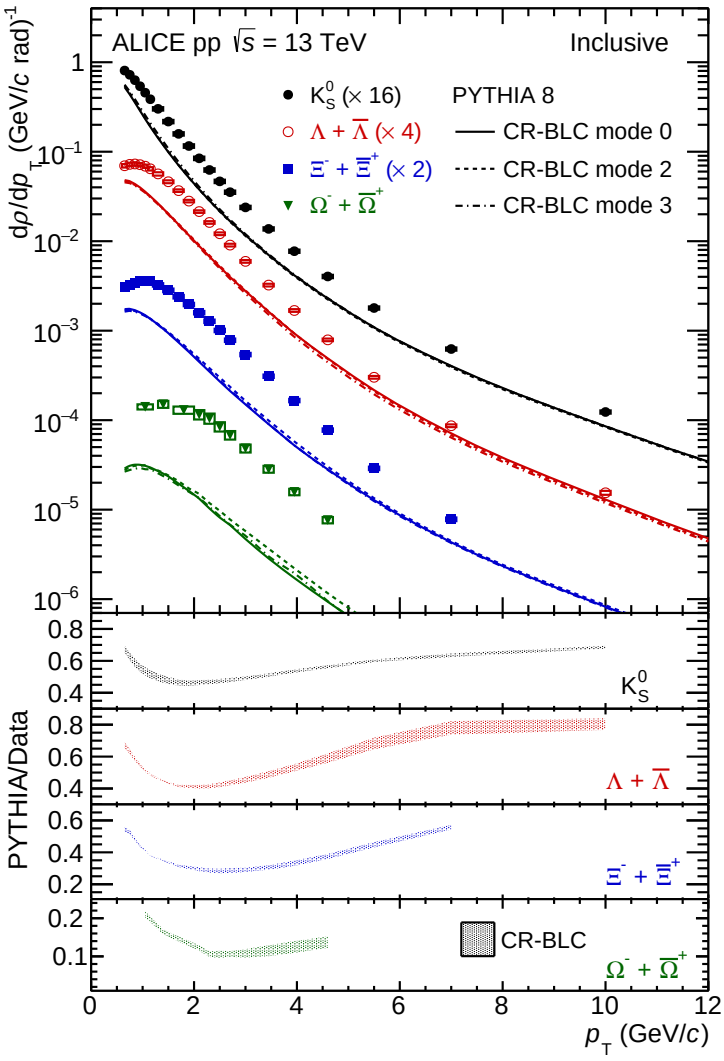

Figure 6: p_{T}-differential density distributions for inclusive $\mathrm{K}^0_{\mathrm{S}}$ (black closed points), Λ (red opened points), Ξ (blue squares) and Ω (green inverted triangles) in pp collisions at $\sqrt{s} = 13$ TeV. The spectra in data are compared with PYTHIA 8 CR-BLC simulations. Three modes, labeled as mode 0 (solid line), 2 (dashed line) and 3 (dashed dot line) are adopted in the simulations. The PYTHIA-to-data ratios are show in the four bottom panels where the three PYTHIA 8 CR-BLC implementation modes are presented as bands. See the text for details.

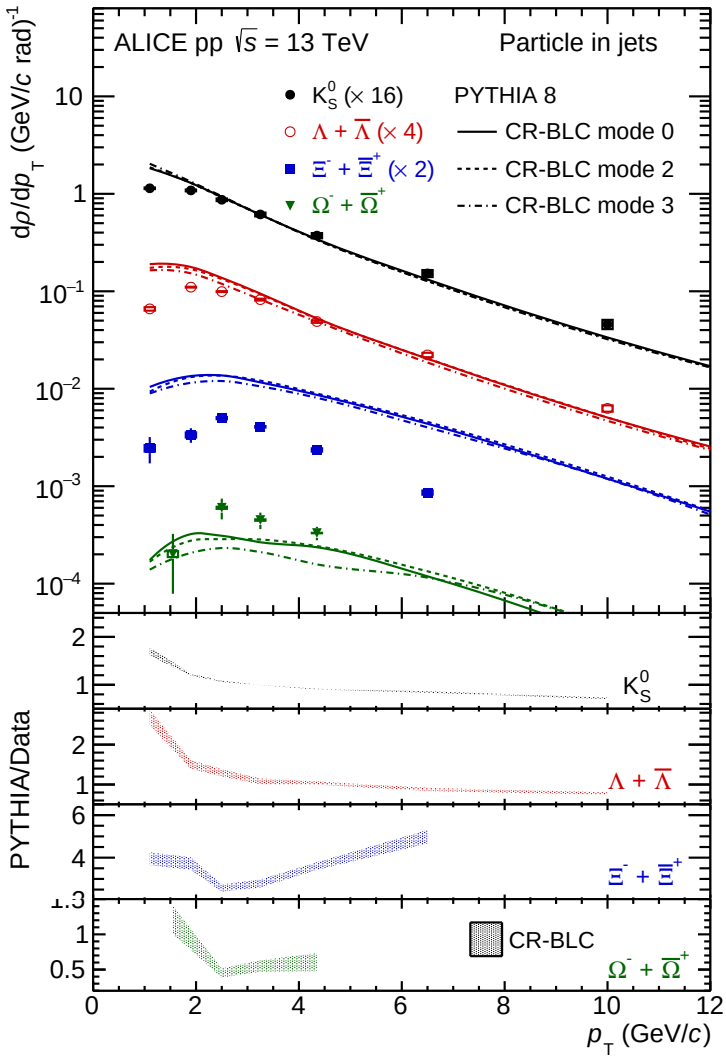

Figure 7: p_{T}-differential density distributions for $\mathrm{K}^0_{\mathrm{S}}$ (black closed points), Λ (red opened points), Ξ (blue squares) and Ω (green inverted triangles) produced within jets in pp collisions at $\sqrt{s} = 13$ TeV. The spectra in data are compared with PYTHIA 8 CR-BLC simulations. Three modes, labeled as mode 0 (solid line), 2 (dashed line) and 3 (dashed dot line) are adopted in the simulations. The PYTHIA-to-data ratios are show in the four bottom panels where the three PYTHIA 8 CR-BLC implementation modes are presented as bands. See the text for details.

However, the Ω/Λ and Ω/Ξ ratios for particles associated with jets show a similar p_{T} dependence as the inclusive particles. The Ω/Λ ratio of JE particles is systematically lower than the inclusive measurement, but with a less suppress than the case of Ξ. The Ω/Ξ ratio of JE particles is compatible with the inclusive measurements within uncertainties. Those phenomena imply the production mechanism of Ω baryons, as strange-quark triplets, in jets may be similar to that in the UE. This behavior has to be further confirmed in the future measurements with improved precision using higher statistics.

The p_{T}-differential densities of inclusive $\mathrm{K}^0_{\mathrm{S}}$, Λ, Ξ and Ω are compared to simulations with PYTHIA 8 event generators [47] in figure 6. For clarity, some of the spectra have been scaled with the factors indicated in the legends. The PYTHIA 8 simulations are performed with the CR-BLC tunes [78], in which the minimisation of the string potential is implemented considering the SU(3) multiplet structure of QCD, allowing for the formation of "baryonic" configurations where two colours can combine coherently to form an anti-colours. In this model, three modes (labeled as mode 0, 2 and 3) are suggested by the authors, applying different constraints on the allowed reconnections among colour sources, in particular concerning the causality connections among strings involved in a reconnection, and time dilation caused by relative boosts of the strings. The density spectra from the PYTHIA 8 simulations are normalized as the same way as data described in section 3.3. The bottom panels of figure 6 present the ratios between PYTHIA 8 simulations and data. Since for each particle specie, the three CR-BLC modes give almost identical p_{T}-differential density spectra, the results corresponding to different CR-BLC modes are presented as bands. And unless explicitly stated, bands will be used to illustrate results related to the PYTHIA 8 CR-BLC modes in the rest of this section.

The inclusive density spectra from PYTHIA 8 simulations underestimate data for all particle species and the p_{T} dependence follows a power-law trend, which does not reproduce the moderate peaks on the spectra at intermediate-p_{T} around 2 GeV/c shown in data. This results the "valley" structures in PYTHIA-to-data ratios in the interval of $1 < p_{\mathrm{T}} < 4$ GeV/c. For $\mathrm{K}^0_{\mathrm{S}}$ and Λ, the value of the ratio reaches the minimum of around 0.4 at $p_{\mathrm{T}} \simeq 2$ GeV/c, then it increases with p_{T} in $p_{\mathrm{T}} > 2$ GeV/c and shows a saturation trend with a value that rises to 0.8 at high-p_{T} in the interval of $p_{\mathrm{T}} > 6$ GeV/c. For the multi-strange baryons, Ξ and Ω, the ratio decrease with strange-quark numbers and baryon masses. The minimum values of the ratio are around 0.2 and 0.1 for Ξ and Ω, respectively.

Figure 7 is similar as figure 6, but it shows the comparisons of p_{T}-differential densities of JE particles to the corresponding PYTHIA 8 simulations. Three different CR-BLC modes also performed in the simulations as well. The JE particle density spectra from PYTHIA 8 simulations are obtained following the same approaches applied to data as detailed in section 3.3. PYTHIA 8 simulations overestimate the density of $\mathrm{K}^0_{\mathrm{S}}$ and Λ in jets in $p_{\mathrm{T}} < 2$ GeV/c, and become closer to data in $p_{\mathrm{T}} > 2$ GeV/c. The difference between data and the simulations for those two particles is almost identical, as seen in the PYTHIA-to-data ratios shown on bottom panels of figure 7. However, the p_{T}-differential density from PYTHIA 8 simulations is slightly softer than data. For Ξ baryons, different from the comparison for inclusive particles, PYTHIA 8 simulations overestimate Ξ production associated with jets over the measured p_{T} range, $0.9 < p_{\mathrm{T}} < 8$ GeV/c, by a factor of around 3 to 6 dependent on p_{T}. A possible explanation is that the strings containing partons produced in the hard scattering processes in PYTHIA fragmentation have stronger string tension. The ss-diquark production rate of those strings is much higher than that in jet fragmentation in data. As the possibility of an ss-diquark combining with another single s-quark to form a Ω baryon is lower than that with u- and d-quarks to form a Ξ baryon, the density of Ω produced in jets is underestimated by PYTHIA 8 simulations over the measured p_{T} range. The corresponding PYTHIA-to-data ratio reaches a value of around 0.5 in $p_{\mathrm{T}} > 2$ GeV/c and is insensitive to p_{T}. Since the production density of Ξ in jets is vastly overestimated by PYTHIA 8 simulations.

The p_{T}-differential particle ratios from the JE and the inclusive selections are compared with the PYTHIA 8 simulations in figure 8. PYTHIA 8 CR-BLC tunes generally agree with the $\Lambda/\mathrm{K}^0_{\mathrm{S}}$ ratios for both JE particles and inclusive measurements, despite the simulations reproduce the individual density spectra neither

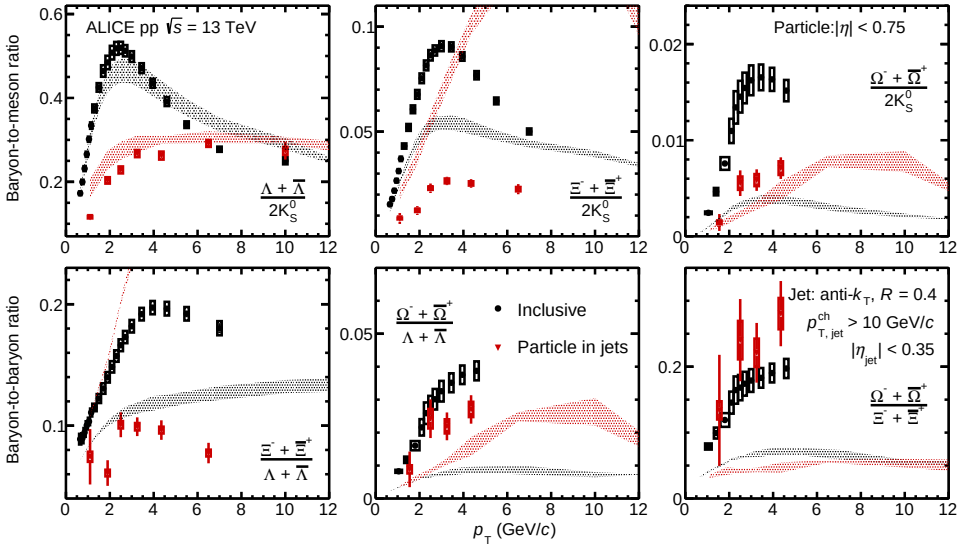

Figure 8: p_{T}-dependent strange baryon-to-meson (top) and baryon-to-baryon (bottom) ratios in pp collisions at $\sqrt{s} = 13$ TeV. For each case, the results of JE (red inverted-triangle) and inclusive (black closed points) particles are compared with PYTHIA 8 CR-BLC simulations. The bands are built by combining the results from the simulations using three different CR-BLC implementation modes. See the text for details.

in jets nor in the inclusive sample. But large discrepancies between data and PYTHIA 8 simulations are observed for all the other cases containing multi-strange hadrons in the numerator over the measured p_{T} acceptance. As stated in [79], although the string junction mechanism applied in PYTHIA 8 CR-BLC tunes increases the baryon production probabilities, the *ss*-diquark is disfavoured in the PYTHIA fragmentation due to the phase-space constrains on high invariant-mass strings. This results in PYTHIA 8 simulations largely underestimating the inclusive particle ratios containing multi-strange hadrons in the numerator. Since the density of Ξ in jets is overestimated by PYTHIA 8 simulations, as a consequence, the $\Xi/\mathrm{K}^0_{\mathrm{S}}$ and Ξ/Λ ratios given by PYTHIA 8 increase dramatically with p_{T} and raise to unreal large values. And in the meantime, the Ω/Ξ ratio in jets is suppressed in the simulations. It seems that PYTHIA 8 simulations qualitatively reproduce the p_{T} dependence for $\Omega/\mathrm{K}^0_{\mathrm{S}}$ and Ω/Λ ratios in jets. However, this may be due to the unrealistic enhancement of the *ss*-diquark produced by strings containing partons from hard scatterings in PYTHIA 8 simulations. The measurements presented in this study provide important constrains on the production mechanisms of particles, especially for those in multi-strange sector, associated with hard partons applied in Monte-Carlo event generators.

4.2 Production and ratios of JE particles in p–Pb collisions at $\sqrt{s_{\mathrm{NN}}} = 5.02$ TeV

The particle to $\pi^{\pm}$ ratios and strange baryon-to-meson ratios measured at high multiplicity in small system (pp and p–Pb) collisions [31–33, 35, 57, 75, 80–82] exhibit an enhancement at intermediate $p_{\mathrm{T}} \sim 3$ GeV/c with respect to the low-multiplicity events, qualitatively reminiscent of that measured in Pb–Pb collisions [34, 83–85]. In the latter, the enhancement is considered as the fingerprint of hydrodynamic evolutions of the color-deconfined matter state, the quark-gluon plasma, created under extreme conditions of high temperature and energy density. To further constrain the particle production mechanisms in small collision systems, the study of strange particle production within charged jets is extended to p–Pb collisions at $\sqrt{s_{\mathrm{NN}}} = 5.02$ TeV in both MB events and in events for various multiplicity intervals.

Figure 9 shows the p_{T}-differential densities of $\mathrm{K}^0_{\mathrm{S}}$, Λ, Ξ and Ω in MB p–Pb collisions at $\sqrt{s_{\mathrm{NN}}} = 5.02$ TeV. For each case, the density distribution of JE particles is compared with that from JC and UE selections, and that of inclusive particles. In general, the particle densities measured in p–Pb collisions have the same order of magnitude as the corresponding ones in pp collisions shown in figure 4. And similar as

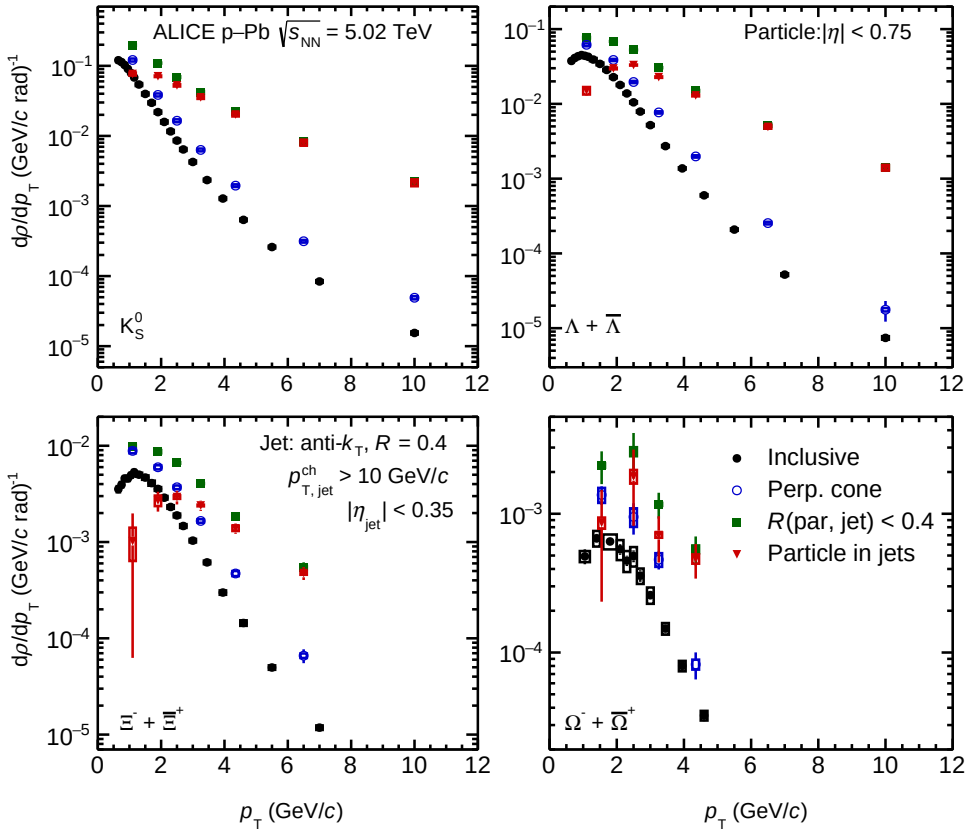

Figure 9: p_{T}-differential density, $\mathrm{d}\rho/\mathrm{d}p_{\mathrm{T}}$, of $\mathrm{K}^0_{\mathrm{S}}$ (top left panel), Λ (top right panel), Ξ (bottom left panel) and Ω (bottom right panel) in p–Pb collisions at $\sqrt{s_{\mathrm{NN}}} = 5.02$ TeV. The spectra of JE particles (red inverted-triangle), associated with hard scatterings, are compared with that of JC (green squares) and UE (blue opened points) selections. The results from inclusive measurements (black closed points) are presented as well.

what observed in pp collisions, the density of JC-selected particles is dominant by that associated with hard scatterings at high p_{T} beyond 3 GeV/c. The p_{T}-dependent density of JE particles is considerably less steep than the inclusive ones due to the trigger of jets. The UE component given by the PC selection is mainly located at low-p_{T} region but the contribution is more significant than in pp collisions. The UE fractions are 61.3% (47.0%), 80.4% (65.5%), 90.0% (73.4%) and 61.4% (62.0%), respectively, for $\mathrm{K}^0_{\mathrm{S}}$, Λ, Ξ in interval of $0.9 < p_{\mathrm{T}} < 1.6$ GeV/c and for Ω in interval of $0.9 < p_{\mathrm{T}} < 2.2$ GeV/c in p–Pb (pp) collisions. This follows the expectation that more associated particles from UE are created with higher energy density of the system. The p_{T}-dependent densities of $\mathrm{K}^0_{\mathrm{S}}$ mesons and, Λ and Ξ baryons with different selections are also measured for various event multiplicity classes, seen figures B.1, B.2 and B.3 in appendix B. The magnitude of the density decreases with the event multiplicity, and the results in the low multiplicity class become almost identical to that in pp collisions. However, the same behavior observed in the MB events is exhibited when comparing the spectra with different selections.

The ratios of JE particles measured in p–Pb collisions at $\sqrt{s_{\mathrm{NN}}} = 5.02$ TeV are shown in figure 10. The results of $\Lambda/\mathrm{K}^0_{\mathrm{S}}$, $\Xi/\mathrm{K}^0_{\mathrm{S}}$ and Ξ/Λ ratios are presented in three event multiplicity classes, from high (0–10%), intermediate (10–40%) to low (40–100%) multiplicities, and compared with that in MB events. Since the multiplicity differential analysis is challenging for Ω baryons due to lack of statistics, therefore, the ratios of $\Omega/\mathrm{K}^0_{\mathrm{S}}$, Ω/Λ and Ω/Ξ are only given in MB events. All the ratios are also compared with the corresponding measurements in pp collisions at $\sqrt{s} = 13$ TeV.

The comparisons between the ratio of JE particles to that of inclusive and UE particles for different

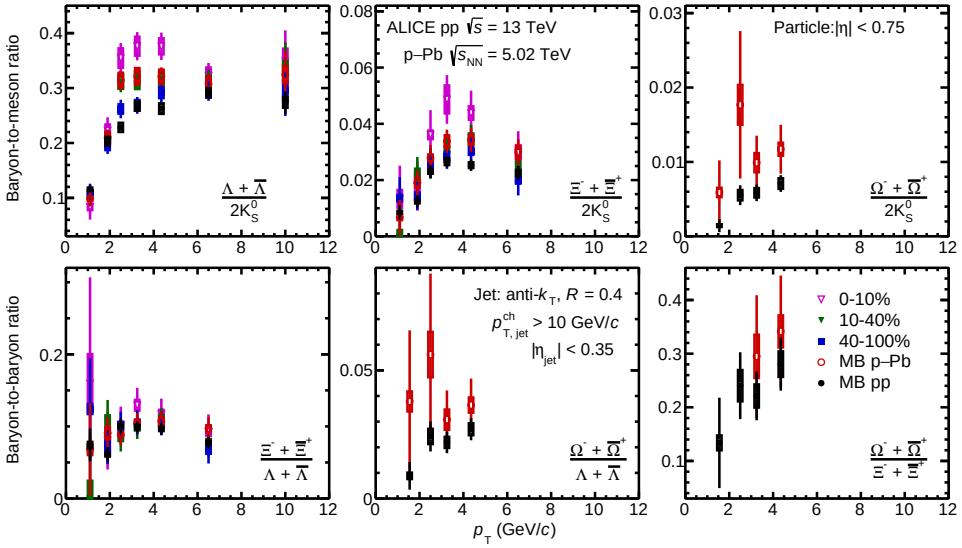

Figure 10: p_{T}-dependent strange baryon-to-meson (top) and baryon-to-baryon (bottom) ratios for particles produced within jets in p–Pb collisions at $\sqrt{s_{\mathrm{NN}}} = 5.02$ TeV. For each case, the results for different event multiplicity classes are compared with that in pp collisions at $\sqrt{s} = 13$ TeV. See the text for details.

event multiplicity classes are shown in figure B.4, B.5 and B.6 in appendix B for $\Lambda/\mathrm{K}^0_{\mathrm{S}}$, $\Xi/\mathrm{K}^0_{\mathrm{S}}$ and Ξ/Λ, respectively. The same as in pp collisions, in each event multiplicity class, p_{T} dependence of the ratio for UE particles is consistent with that of inclusive particles within uncertainties, and the enhancement in the ratio of inclusive particles at intermediate p_{T} is not presented in jets, illustrating that the flow-like enhancement on particle ratios observed at high multiplicity in small systems is raised by UE but not by the jet fragmentation.

5 Summary

The production of $\mathrm{K}^0_{\mathrm{S}}$ meons and Λ, Ξ and Ω baryons is measured separately for particles associated with hard scatterings and the underlying event for the first time at the LHC in pp collisions at $\sqrt{s} = 13$ TeV and p–Pb collisions at $\sqrt{s_{\mathrm{NN}}} = 5.02$ TeV. The results in pp collisions are compared with those obtained in PYTHIA 8 CR-BLC simulations. PYTHIA 8 simulations fairly reproduce the $\Lambda/\mathrm{K}^0_{\mathrm{S}}$ ratio in data. However, large discrepancies between data and simulations are observed if in the ratios including multi-strange baryons. The strange baryon-to-meson and baryon-to-baryon ratios associated with jets in p–Pb collisions is insensitive to the event multiplicity and consistent with the ratio measured in pp collisions. The enhancement in the ratio at intermediate p_{T} found in the inclusive particle measurements in high multiplicity p–Pb and Pb–Pb collisions is not present for particles associated with hard scatterings tagged by jets reconstructed from charged particles for $p_{\mathrm{T,jet}}^{\mathrm{ch}} > 10$ GeV/c in p–Pb and pp collisions. Moreover, as the enhancement has been linked to the interplay of radial flow and parton recombination at intermediate p_{T}, its absence within the jet cone demonstrates that these effects are indeed limited to the soft particle production processes.

Acknowledgements

References

[1] J. Rafelski and R. Hagedorn, "From hadron gas to quark matter, 2",. https://cds.cern.ch/record/126179.

[2] H. Satz, "Color deconfinement in nuclear collisions", *Rept. Prog. Phys.* **63** (2000) , arXiv:hep-ph/0007069.

[3] E. V. Shuryak, "Theory and phenomenology of the QCD vacuum", *Phys. Rept.* **115** (1984) .

[4] B. V. Jacak and B. Muller, "The exploration of hot nuclear matter", *Science* **337** (2012) .

[5] J. Cleymans, R. Gavai, and E. Suhonen, "Quarks and Gluons at High Temperatures and Densities", *Phys. Rept.* **130** (1986) .

[6] S. Bass, M. Gyulassy, H. Stoecker, and W. Greiner, "Signatures of quark gluon plasma formation in high-energy heavy ion collisions: A Critical review", *J. Phys. G* **25** (1999) , arXiv:hep-ph/9810281.

[7] P. Braun-Munzinger and J. Stachel, "The quest for the quark-gluon plasma", *Nature* **448** (2007) .

[8] E. Laermann and O. Philipsen, "The Status of lattice QCD at finite temperature", *Ann. Rev. Nucl. Part. Sci.* **53** (2003) , arXiv:hep-ph/0303042.

[9] S. Gupta, X. Luo, B. Mohanty, H. G. Ritter, and N. Xu, "Scale for the Phase Diagram of Quantum Chromodynamics", *Science* **332** (2011) , arXiv:1105.3934 [hep-ph].

[10] T. Bhattacharya *et al.*, "QCD Phase Transition with Chiral Quarks and Physical Quark Masses", *Phys. Rev. Lett.* **113** no. 8, (2014) , arXiv:1402.5175 [hep-lat].

[11] C. Salgado *et al.*, "Proton-Nucleus Collisions at the LHC: Scientific Opportunities and Requirements", *J. Phys. G* **39** (2012) , arXiv:1105.3919 [hep-ph].

[12] K. J. Eskola, P. Paakkinen, H. Paukkunen, and C. A. Salgado, "EPPS16: Nuclear parton distributions with LHC data", *Eur. Phys. J. C* **77** no. 3, (2017) , arXiv:1612.05741 [hep-ph].

[13] Z. Yang, W. Chen, Y. He, W. Ke, L. Pang, and X.-N. Wang, "Search for the elusive jet-induced diffusion wake in Z/γ-jets with 2D jet tomography in high-energy heavy-ion collisions", arXiv:2101.05422 [hep-ph].

[14] W. Zhao, W. Ke, W. Chen, T. Luo, and X.-N. Wang, "From hydro to jet quenching, coalescence and hadron cascade: a coupled approach to solving the $R_{\rm AA} \otimes v_2$ puzzle", arXiv:2103.14657 [hep-ph].

[15] W. Chen, S. Cao, T. Luo, L.-G. Pang, and X.-N. Wang, "The effect of jet-induced medium excitation on Λ/K^0_S in jet in Pb–Pb collisions", *Nucl. Phys. A* **1005** (2021) .

[16] Y. Tachibana, N.-B. Chang, and G.-Y. Qin, "Full jet in quark-gluon plasma with hydrodynamic medium response", *Phys. Rev. C* **95** no. 4, (2017) , arXiv:1701.07951 [nucl-th].

[17] W. Chen, S. Cao, T. Luo, L.-G. Pang, and X.-N. Wang, "Effects of jet-induced medium excitation in γ-hadron correlation in A+A collisions", *Phys. Lett. B* **777** (2018) , arXiv:1704.03648 [nucl-th].

[18] D. de Florian, R. Sassot, and M. Stratmann, "Global analysis of fragmentation functions for protons and charged hadrons", *Phys. Rev. D* **76** (2007) , arXiv:0707.1506 [hep-ph].

[19] D. d'Enterria, K. J. Eskola, I. Helenius, and H. Paukkunen, "Confronting current NLO parton fragmentation functions with inclusive charged-particle spectra at hadron colliders", *Nucl. Phys. B* **883** (2014) , arXiv:1311.1415 [hep-ph].

[20] D. de Florian, R. Sassot, M. Epele, R. J. Hernández-Pinto, and M. Stratmann, "Parton-to-Pion Fragmentation Reloaded", *Phys. Rev. D* **91** no. 1, (2015) , arXiv:1410.6027 [hep-ph].

[21] D. de Florian, M. Epele, R. J. Hernandez-Pinto, R. Sassot, and M. Stratmann, "Parton-to-Kaon Fragmentation Revisited", *Phys. Rev. D* **95** no. 9, (2017) , arXiv:1702.06353 [hep-ph].

[22] K. J. Eskola, H. Paukkunen, and C. A. Salgado, "EPS09: A New Generation of NLO and LO Nuclear Parton Distribution Functions", *JHEP* **04** (2009) , arXiv:0902.4154 [hep-ph].

[23] B. Z. Kopeliovich, J. Nemchik, A. Schafer, and A. V. Tarasov, "Cronin effect in hadron production off nuclei", *Phys. Rev. Lett.* **88** (2002) , arXiv:hep-ph/0201010.

[24] I. Vitev, "Non-Abelian energy loss in cold nuclear matter", *Phys. Rev. C* **75** (2007) , arXiv:hep-ph/0703002.

[25] **ALICE** Collaboration, S. Acharya *et al.*, "Investigations of Anisotropic Flow Using Multiparticle Azimuthal Correlations in pp, p-Pb, Xe-Xe, and Pb-Pb Collisions at the LHC", *Phys. Rev. Lett.* **123** no. 14, (2019) , arXiv:1903.01790 [nucl-ex].

[26] **ATLAS** Collaboration, G. Aad *et al.*, "Observation of Long-Range Elliptic Azimuthal Anisotropies in $\sqrt{s}$ =13 and 2.76 TeV pp Collisions with the ATLAS Detector", *Phys. Rev. Lett.* **116** no. 17, (2016) , arXiv:1509.04776 [hep-ex].

[27] **ALICE** Collaboration, B. Abelev *et al.*, "Long-range angular correlations on the near and away side in p-Pb collisions at $\sqrt{s_{NN}} = 5.02$ TeV", *Phys. Lett. B* **719** (2013) , arXiv:1212.2001 [nucl-ex].

[28] **ALICE** Collaboration, B. B. Abelev *et al.*, "Long-range angular correlations of π, K and p in p-Pb collisions at $\sqrt{s_{\rm NN}}$ = 5.02 TeV", *Phys. Lett. B* **726** (2013) , arXiv:1307.3237 [nucl-ex].

[29] **CMS** Collaboration, V. Khachatryan *et al.*, "Evidence for Collective Multiparticle Correlations in p-Pb Collisions", *Phys. Rev. Lett.* **115** no. 1, (2015) , arXiv:1502.05382 [nucl-ex].

[30] **ALICE** Collaboration, B. B. Abelev *et al.*, "$K^*(892)^0$ and $\phi(1020)$ production in Pb-Pb collisions at $\sqrt{sNN}$ = 2.76 TeV", *Phys. Rev. C* **91** (2015) , arXiv:1404.0495 [nucl-ex].

[31] **ALICE** Collaboration, J. Adam *et al.*, "Multi-strange baryon production in p–Pb collisions at $\sqrt{s_{\rm NN}} = 5.02$ TeV", *Phys. Lett. B* **758** (2016) , arXiv:1512.07227 [nucl-ex].

[32] **ALICE** Collaboration, S. Acharya *et al.*, "Multiplicity dependence of light-flavor hadron production in pp collisions at $\sqrt{s}$ = 7 TeV", *Phys. Rev.* **C99** no. 2, (2019) , arXiv:1807.11321 [nucl-ex].

[33] **CMS** Collaboration, V. Khachatryan *et al.*, "Multiplicity and rapidity dependence of strange hadron production in pp, p–Pb, and Pb–Pb collisions at the LHC", *Phys. Lett.* **B768** (2017) , arXiv:1605.06699 [nucl-ex].

[34] **ALICE** Collaboration, B. B. Abelev *et al.*, "$K^0_{\rm S}$ and Λ production in Pb–Pb collisions at $\sqrt{s_{\rm NN}} = 2.76$ TeV", *Phys. Rev. Lett.* **111** (2013) , arXiv:1307.5530 [nucl-ex].

[35] **ALICE** Collaboration, J. Adam *et al.*, "Enhanced production of multi-strange hadrons in high-multiplicity proton–proton collisions", *Nature Phys.* **13** (2017) , arXiv:1606.07424 [nucl-ex].

[36] **ALICE** Collaboration, B. B. Abelev *et al.*, "Multiplicity Dependence of Pion, Kaon, Proton and Lambda Production in p-Pb Collisions at $\sqrt{s_{NN}}$ = 5.02 TeV", *Phys. Lett. B* **728** (2014) , arXiv:1307.6796 [nucl-ex].

[37] **ALICE** Collaboration, S. Acharya *et al.*, "Measurements of inclusive jet spectra in pp and central Pb-Pb collisions at $\sqrt{s_{\rm NN}}$ = 5.02 TeV", *Phys. Rev. C* **101** no. 3, (2020) , arXiv:1909.09718 [nucl-ex].

[38] **ALICE** Collaboration, S. Acharya *et al.*, "Measurement of charged jet cross section in pp collisions at $\sqrt{s} = 5.02$ TeV", *Phys. Rev. D* **100** no. 9, (2019) , arXiv:1905.02536 [nucl-ex].

[39] **ALICE** Collaboration, B. B. Abelev *et al.*, "Charged jet cross sections and properties in proton-proton collisions at $\sqrt{s} = 7$ TeV", *Phys. Rev. D* **91** no. 11, (2015) , arXiv:1411.4969 [nucl-ex].

[40] **ALICE** Collaboration, B. Abelev *et al.*, "Measurement of the inclusive differential jet cross section in pp collisions at $\sqrt{s} = 2.76$ TeV", *Phys. Lett. B* **722** (2013) , arXiv:1301.3475 [nucl-ex].

[41] **ALICE** Collaboration, S. Acharya *et al.*, "Charged jet cross section and fragmentation in proton-proton collisions at $\sqrt{s}$ = 7 TeV", *Phys. Rev. D* **99** no. 1, (2019) , arXiv:1809.03232 [nucl-ex].

[42] **ALICE** Collaboration, S. Acharya *et al.*, "Constraints on jet quenching in p-Pb collisions at $\sqrt{s_{\rm NN}}$ = 5.02 TeV measured by the event-activity dependence of semi-inclusive hadron-jet distributions", *Phys. Lett. B* **783** (2018) , arXiv:1712.05603 [nucl-ex].

[43] **ALICE** Collaboration, J. Adam *et al.*, "Measurement of dijet k_T in p–Pb collisions at $\sqrt{s_{NN}}$=5.02 TeV", *Phys. Lett. B* **746** (2015) , arXiv:1503.03050 [nucl-ex].

[44] **ALICE** Collaboration, J. Adam *et al.*, "Centrality dependence of charged jet production in p–Pb collisions at $\sqrt{s_{\rm NN}}$ = 5.02 TeV", *Eur. Phys. J. C* **76** no. 5, (2016) , arXiv:1603.03402 [nucl-ex].

[45] **ALICE** Collaboration, S. Acharya *et al.*, "Constraints on jet quenching in p-Pb collisions at $\sqrt{s_{\rm NN}}$ = 5.02 TeV measured by the event-activity dependence of semi-inclusive hadron-jet distributions", *Phys. Lett. B* **783** (2018) , arXiv:1712.05603 [nucl-ex].

[46] **ALICE** Collaboration, S. Acharya *et al.*, "Production of Λ and K^0_S in jets in p-Pb collisions at $\sqrt{s_{\rm NN}} = 5$ TeV and pp collisions at $\sqrt{s} = 7$ TeV", arXiv:2105.04890 [nucl-ex].

[47] T. Sjöstrand, S. Ask, J. R. Christiansen, R. Corke, N. Desai, P. Ilten, S. Mrenna, S. Prestel, C. O. Rasmussen, and P. Z. Skands, "An introduction to PYTHIA 8.2", *Comput. Phys. Commun.* **191** (2015) , arXiv:1410.3012 [hep-ph].

[48] **ALICE** Collaboration, K. Aamodt *et al.*, "The ALICE experiment at the CERN LHC", *Journal of Instrumentation* **3** no. 08, (Aug, 2008) .

[49] **ALICE** Collaboration, B. B. Abelev *et al.*, "Performance of the ALICE Experiment at the CERN LHC", *Int. J. Mod. Phys. A* **29** (2014) , arXiv:1402.4476 [nucl-ex].

[50] **ALICE** Collaboration, E. Abbas *et al.*, "Performance of the ALICE VZERO system", *JINST* **8** (2013) , arXiv:1306.3130 [nucl-ex].

[51] **ALICE** Collaboration, K. Aamodt *et al.*, "Alignment of the ALICE Inner Tracking System with cosmic-ray tracks", *JINST* **5** (2010) , arXiv:1001.0502 [physics.ins-det].

[52] J. Alme *et al.*, "The ALICE TPC, a large 3-dimensional tracking device with fast readout for ultra-high multiplicity events", *Nucl. Instrum. Meth. A* **622** (2010) , arXiv:1001.1950 [physics.ins-det].

[53] **ALICE TOF** Collaboration, A. Akindinov *et al.*, "Particle identification with the ALICE TOF detector at very high particle multiplicity", *Eur. Phys. J. C* **32S1** (2004) .

[54] A. Akindinov *et al.*, "The ALICE Time-Of-Flight system: Construction, assembly and quality tests", *Nuovo Cim. B* **124** (2009) .

[55] A. Akindinov *et al.*, "Results of the ALICE time-of-flight detector from the 2009 cosmic-ray data taking", *Eur. Phys. J. C* **68** (2010) .

[56] **ALICE** Collaboration, F. Carnesecchi, "Performance of the ALICE Time-Of-Flight detector at the LHC", *JINST* **14** no. 06, (2019) , arXiv:1806.03825 [physics.ins-det].

[57] **ALICE** Collaboration, S. Acharya *et al.*, "Production of light-flavor hadrons in pp collisions at $\sqrt{s} = 7$ and $\sqrt{s} = 13$ TeV", *Eur. Phys. J.* **C81** no. 3, (2021) , arXiv:2005.11120 [nucl-ex].

[58] **ALICE** Collaboration, N. Jacazio, "PID performance of the ALICE-TOF detector at Run 2", *PoS* **LHCP2018** (2018) , arXiv:1809.00574 [physics.ins-det].

[59] **ALICE Collaboration** Collaboration, "ALICE luminosity determination for pp collisions at $\sqrt{s} = 13$ TeV", Jun, 2016. http://cds.cern.ch/record/2160174.

[60] **ALICE** Collaboration, "Measurement of visible cross sections in proton-lead collisions at $\sqrt{s_{\rm NN}}$ = 5.02 tev in van der meer scans with the alice detector", *Journal of Instrumentation* **9** no. 11, (Nov, 2014) . http://dx.doi.org/10.1088/1748-0221/9/11/P11003.

[61] **ALICE** Collaboration, S. Acharya *et al.*, "Azimuthal correlations of prompt D mesons with charged particles in pp and p–Pb collisions at $\sqrt{s_{NN}}$ = 5.02 TeV", *Eur. Phys. J. C* **80** no. 10, (2020) , arXiv:1910.14403 [nucl-ex].

[62] **ALICE** Collaboration, J. Adam *et al.*, "Pseudorapidity and transverse-momentum distributions of charged particles in proton-proton collisions at $\sqrt{s} = 13$ TeV", *Phys. Lett. B* **753** (2016) , arXiv:1509.08734 [nucl-ex].

[63] M. Cacciari, G. P. Salam, and G. Soyez, "FastJet User Manual", *Eur. Phys. J. C* **72** (2012) , arXiv:1111.6097 [hep-ph].

[64] M. Cacciari, G. P. Salam, and G. Soyez, "The anti-k_t jet clustering algorithm", *JHEP* **04** (2008) , arXiv:0802.1189 [hep-ph].

[65] S. Catani, Y. L. Dokshitzer, M. H. Seymour, and B. R. Webber, "Longitudinally invariant K_t clustering algorithms for hadron hadron collisions", *Nucl. Phys. B* **406** (1993) .

[66] S. D. Ellis and D. E. Soper, "Successive combination jet algorithm for hadron collisions", *Phys. Rev. D* **48** (1993) , arXiv:hep-ph/9305266.

[67] M. Cacciari and G. P. Salam, "Pileup subtraction using jet areas", *Phys. Lett. B* **659** (2008) , arXiv:0707.1378 [hep-ph].

[68] M. Cacciari, G. P. Salam, and G. Soyez, "The Catchment Area of Jets", *JHEP* **04** (2008) , arXiv:0802.1188 [hep-ph].

[69] **CMS** Collaboration, S. Chatrchyan *et al.*, "Measurement of the underlying event activity in pp collisions at $\sqrt{s} = 0.9$ and 7 TeV with the novel jet-area/median approach", *JHEP* **08** (2012) , arXiv:1207.2392 [hep-ex].

[70] **ALICE** Collaboration, J. Adam *et al.*, "Measurement of charged jet production cross sections and nuclear modification in p-Pb collisions at $\sqrt{s_{\rm NN}} = 5.02$ TeV", *Phys. Lett. B* **749** (2015) , arXiv:1503.00681 [nucl-ex].

[71] **ALICE** Collaboration, J. Adam *et al.*, "Centrality dependence of charged jet production in p–Pb collisions at $\sqrt{s_{\rm NN}} = 5.02$ TeV", *Eur. Phys. J. C* **76** no. 5, (2016) , arXiv:1603.03402 [nucl-ex].

[72] **Particle Data Group** Collaboration, M. Tanabashi *et al.*, "Review of Particle Physics", *Phys. Rev. D* **98** (Aug, 2018) .

[73] **ALICE** Collaboration, K. Aamodt *et al.*, "Strange particle production in proton-proton collisions at sqrt(s) = 0.9 TeV with ALICE at the LHC", *Eur. Phys. J. C* **71** (2011) , arXiv:1012.3257 [hep-ex].

[74] **ALICE** Collaboration, B. Abelev *et al.*, "Multi-strange baryon production in pp collisions at $\sqrt{s} = 7$ TeV with ALICE", *Phys. Lett.* **B712** (2012) , arXiv:1204.0282 [nucl-ex].

[75] **ALICE** Collaboration, S. Acharya *et al.*, "Multiplicity dependence of (multi-)strange hadron production in proton–proton collisions at $\sqrt{s} = 13$ TeV", *Eur. Phys. J.* **C80** no. 2, (2020) , arXiv:1908.01861 [nucl-ex].

[76] S. Roesler, R. Engel, and J. Ranft, "The Monte Carlo event generator DPMJET-III", in *International Conference on Advanced Monte Carlo for Radiation Physics, Particle Transport Simulation and Applications (MC 2000)*, pp. 1033–1038. 12, 2000. arXiv:hep-ph/0012252.

[77] R. Brun, F. Bruyant, F. Carminati, S. Giani, M. Maire, A. McPherson, G. Patrick, and L. Urban, "GEANT Detector Description and Simulation Tool",.

[78] J. R. Christiansen and P. Z. Skands, "String Formation Beyond Leading Colour", *JHEP* **08** (2015) , arXiv:1505.01681 [hep-ph].

[79] C. Bierlich and J. R. Christiansen, "Effects of color reconnection on hadron flavor observables", *Phys. Rev.* **D92** no. 9, (2015) , arXiv:1507.02091 [hep-ph].

[80] **ALICE** Collaboration, S. Acharya *et al.*, "Production of charged pions, kaons, and (anti-)protons in Pb–Pb and inelastic pp collisions at $\sqrt{s_{\rm NN}} = 5.02$ TeV", *Phys. Rev.* **C101** no. 4, (2020) , arXiv:1910.07678 [nucl-ex].

[81] **ALICE** Collaboration, B. B. Abelev *et al.*, "Multiplicity Dependence of Pion, Kaon, Proton and Lambda Production in p-Pb Collisions at $\sqrt{s_{\rm NN}} = 5.02$ TeV", *Phys. Lett.* **B728** (2014) , arXiv:1307.6796 [nucl-ex].

[82] **ALICE** Collaboration, J. Adam *et al.*, "Multiplicity dependence of charged pion, kaon, and (anti)proton production at large transverse momentum in p-Pb collisions at $\sqrt{s_{\rm NN}} = 5.02$ TeV", *Phys. Lett. B* **760** (2016) , arXiv:1601.03658 [nucl-ex].

[83] **ALICE** Collaboration, B. Abelev *et al.*, "Pion, Kaon, and Proton Production in Central Pb–Pb Collisions at $\sqrt{s_{\rm NN}} = 2.76$ TeV", *Phys. Rev. Lett.* **109** (2012) , arXiv:1208.1974 [hep-ex].

[84] **ALICE** Collaboration, B. Abelev *et al.*, "Centrality dependence of π, K, p production in Pb–Pb collisions at $\sqrt{s_{\rm NN}} = 2.76$ TeV", *Phys. Rev.* **C88** (2013) , arXiv:1303.0737 [hep-ex].

[85] **ALICE** Collaboration, B. B. Abelev *et al.*, "Multi-strange baryon production at mid-rapidity in Pb–Pb collisions at $\sqrt{s_{\rm NN}} = 2.76$ TeV", *Phys. Lett.* **B728** (2014) , arXiv:1307.5543 [nucl-ex]. [Erratum: Phys.Lett.B 734, 409–410 (2014)].

A Particle candidate selection criteria

Table A.1: K^0_S (Λ and $\overline{\Lambda}$) candidate selection criteria of topological variables, daughter tracks and V^0 candidates. The DCA stands for the "Distance of Closest Approach", PV represents the "Primary collision Vertex" and CPA is the "Cosine Pointing Angle between the momentum vector of the reconstructed V^0 and the displacement vector between the decay and primary vertices".

Topological variable	**pp**	**p–Pb**
V^0 transverse decay radius	> 0.5 cm	> 0.5 cm
DCA of positive / negative track to PV	> 0.06 cm	> 0.06 cm
DCA between V^0 daughter tracks	$< 1.0\sigma$	$< 1\sigma$
CPA of V^0	> 0.97 (0.995)	> 0.97 (0.995)
Track selection		
Daughter track pseudo-rapidity interval	$\|\eta\| < 0.8$	$\|\eta\| < 0.8$
Daughter track $N_{\text{crossed rows}}$	≥ 70	≥ 70
Daughter Track $N_{\text{crossed rows}}/N_{\text{findable}}$	≥ 0.8	≥ 0.8
TPC $\mathrm{d}E/\mathrm{d}x$	$< 5\sigma$	$< 5\sigma$
Candidate selection		
Pseudo-rapidity interval	$\|\eta\| < 0.75$	$\|\eta\| < 0.75$
Proper lifetime(mL/p)	< 20 (30) cm	< 20 (30) cm
Competing mass	> 0.005 (0.010) GeV/c^2	> 0.005 (0.010) GeV/c^2

Table A.2: $\Xi^{\pm}$ ($\Omega^{\pm}$) candidate selection criteria of topological variables, daughter tracks and cascade candidates.

Topological variable	**pp**	**p–Pb**
Cascade transverse decay radius	$> 0.8(0.6)$ cm	> 0.6 cm
V^0 transverse decay radius	> 1.4 cm	> 1.2 cm
DCA (bachelor to PV)	> 0.05 cm	> 0.04 cm
DCA (V^0 to PV)	> 0.07 cm	> 0.06 cm
DCA (positive / negative track to PV)	$> 0.04(0.03)$ cm	> 0.03 cm
DCA between V^0 daughter tracks	$< 1.6\sigma$	$< 1.5\sigma$
DCA (bachelor to V^0)	$< 1.6(1.0)$ cm	< 1.3 cm
CPA of Cascade	> 0.97	> 0.97
CPA of V^0	> 0.97	> 0.97
V^0 invariant mass window	± 0.006 GeV/c^2	± 0.008 GeV/c^2
Track selection		
Daughter track pseudo-rapidity interval	$\|\eta\| < 0.8$	$\|\eta\| < 0.8$
Daughter track $N_{\text{crossed rows}}$	≥ 70	≥ 70
Daughter Track $N_{\text{crossed rows}}/N_{\text{findable}}$	≥ 0.8	≥ 0.8
TPC $\mathrm{d}E/\mathrm{d}x$	$< 5\sigma$	$< 4\sigma$
Candidate selection		
Pseudo-rapidity interval	$\|\eta\| < 0.75$	$\|\eta\| < 0.75$
Proper lifetime (mL/p)		$< 3 \times c\tau$
Competing mass	8 MeV/c^2	8 MeV/c^2

B p_{T}-differential particle density and ratios for event multiplicity classes in p–Pb collisions at $\sqrt{s_{\mathrm{NN}}} = 5.02$ TeV

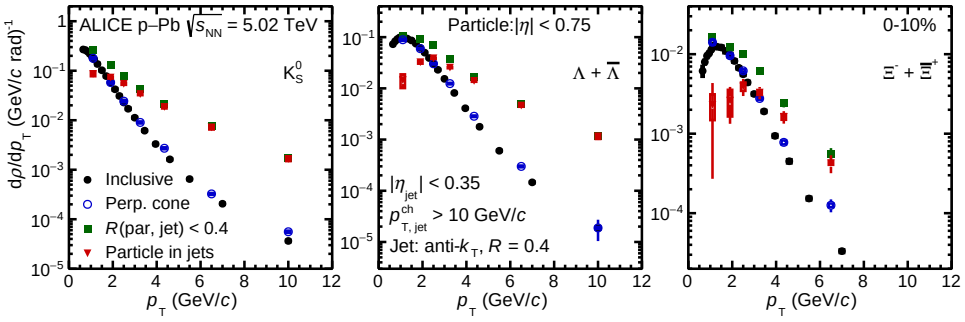

Figure B.1: p_{T}-differential density, $\mathrm{d}\rho/\mathrm{d}p_{\mathrm{T}}$, of $\mathrm{K}^0_{\mathrm{S}}$ (left panel), Λ (middle panel) and Ξ (right panel) for the 0–10% event multiplicity class in p–Pb collisions at $\sqrt{s_{\mathrm{NN}}} = 5.02$ TeV. The spectra of JE particles (red inverted-triangle), associated with hard scatterings, are compared with that of JC (green squares) and UE (blue opened points) selections. The results from inclusive measurements (black closed points) are presented as well.

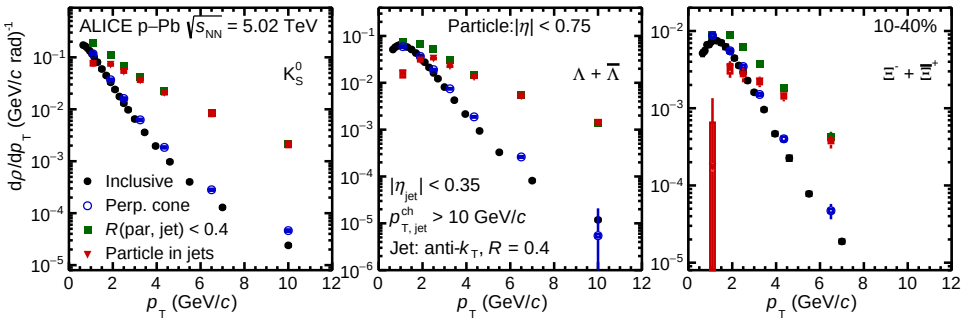

Figure B.2: p_{T}-differential density, $\mathrm{d}\rho/\mathrm{d}p_{\mathrm{T}}$, of $\mathrm{K}^0_{\mathrm{S}}$ (left panel), Λ (middle panel) and Ξ (right panel) for the 10–40% event multiplicity class in p–Pb collisions at $\sqrt{s_{\mathrm{NN}}} = 5.02$ TeV. The spectra of JE particles (red inverted-triangle), associated with hard scatterings, are compared with that of JC (green squares) and UE (blue opened points) selections. The results from inclusive measurements (black closed points) are presented as well.

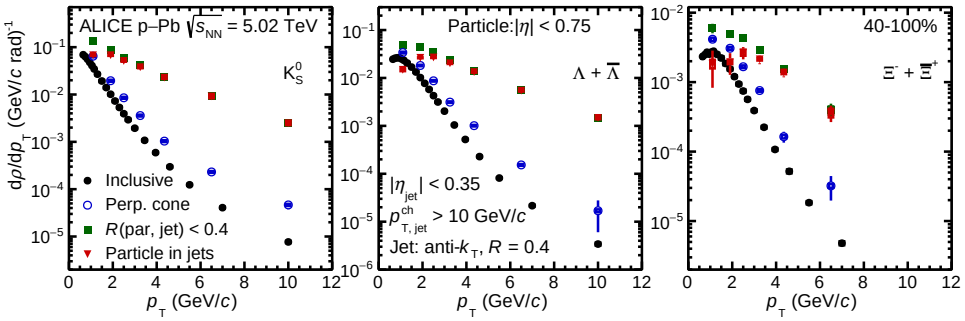

Figure B.3: p_{T}-differential density, $\mathrm{d}\rho/\mathrm{d}p_{\mathrm{T}}$, of $\mathrm{K}^0_{\mathrm{S}}$ (left panel), Λ (middle panel) and Ξ (right panel) for the 40–100% event multiplicity class in p–Pb collisions at $\sqrt{s_{\mathrm{NN}}} = 5.02$ TeV. The spectra of JE particles (red inverted-triangle), associated with hard scatterings, are compared with that of JC (green squares) and UE (blue opened points) selections. The results from inclusive measurements (black closed points) are presented as well.

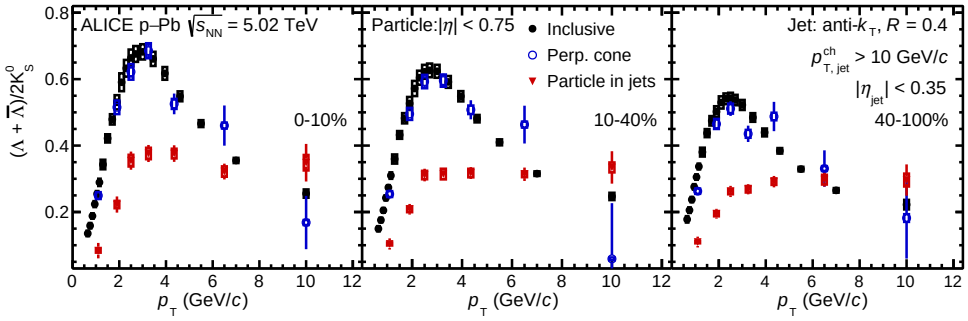

Figure B.4: p_{T}-dependent $\Lambda/\mathrm{K}^0_{\mathrm{S}}$ ratio for 0–10% (left panel), 10–40% (middle panel) and 40–100% (right panel) event multiplicity classes. For each case, the results of JE particles (red inverted-triangle) are compared with that of inclusive (black closed points) and UE (blue opened points) particles.

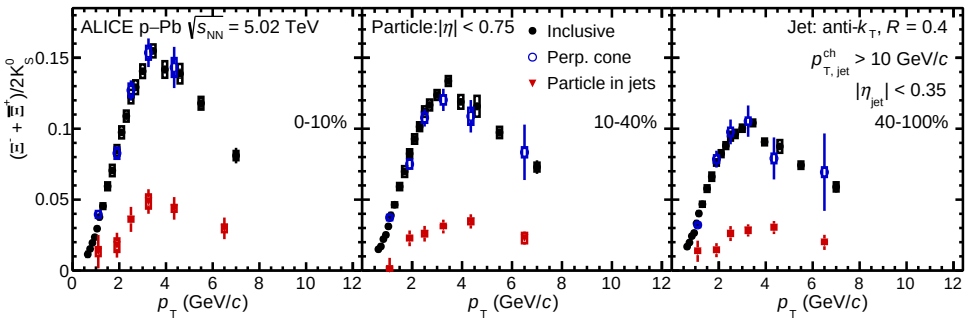

Figure B.5: p_{T}-dependent $\Xi/\mathrm{K}^0_{\mathrm{S}}$ ratio for 0–10% (left panel), 10–40% (middle panel) and 40–100% (right panel) event multiplicity classes. For each case, the results of JE particles (red inverted-triangle) are compared with that of inclusive (black closed points) and UE (blue opened points) particles.

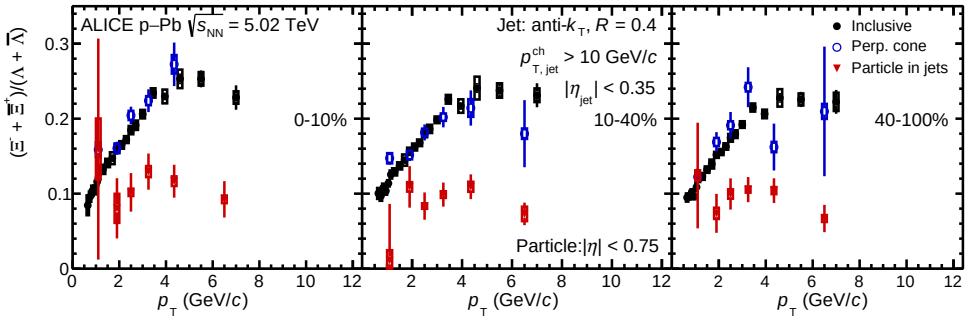

Figure B.6: p_{T}-dependent Ξ/Λ ratio for 0–10% (left panel), 10–40% (middle panel) and 40–100% (right panel) event multiplicity classes. For each case, the results of JE particles (red inverted-triangle) are compared with that of inclusive (black closed points) and UE (blue opened points) particles.

C The ALICE Collaboration